이학박사 학위논문

Electrical and Photoswitching Properties of Large-Area Molecular Monolayer Junctions with Graphene Electrodes

그래핀 전극 기반 대면적 단분자박막 분자접합의 전기적 특성 및 광스위칭 현상에 대한 연구

2020 년 2 월

서울대학교 대학원

물리·천문학부

장 연 식

Electrical and Photoswitching Properties of Large-Area Molecular Monolayer Junctions with Graphene Electrodes

그래핀 전극 기반 대면적 단분자박막 분자접합의
전기적 특성 및 광스위칭 현상에 대한 연구

지도교수 이 탁 희

이 논문을 이학박사 학위논문으로 제출함
2020 년 1 월

서울대학교 대학원
물리천문학부
장 연 식

장연식의 이학박사 학위논문을 인준함
2019 년 12 월

위 원 장 홍 승 훈 (인)
부위원장 이 탁 희 (인)
위 원 김 창 영 (인)
위 원 박 철 환 (인)
위 원 김 태 욱 (인)

Abstract

Electrical and Photoswitching Properties of Large-Area Molecular Monolayer Junctions with Graphene Electrodes

Yeonsik Jang
Department of Physics and Astronomy
Seoul National University

Molecular electronics uses a single molecule or self-assembled monolayer (SAM) as active component of electrical devices such as rectifier, transistor, switch, memory, circuit, etc. Its aim is to reach ultimate miniaturization of integrated electronic devices, surpassing the limitation of silicon based electronics. Molecular electronic devices have remarkable advantages such that functional molecules can be used as building-block with low cost, high throughput, and simple synthesis process. However, there are also many challenges in molecular electronics, because of its low device stability, reliability, and reproducibility. Furthermore, its charge transport nature and electrode-metal interface characteristics are not fully understood. Therefore, fabrication of reliable molecular electronics junctions and investigation of its charge transport characteristics are demanded for the practical molecular devices in future.

In this regards, first, I fabricated high-yield and reliable benzenedithiolate molecular junctions with graphene electrodes and investigated the electrical properties of the junctions. I studied length- and temperature- dependent electrical properties of the molecular junctions, from which it was shown that the main conduction mechanism was non-resonant tunneling. Also I investigated the reliability of the junctions under mechanical bending environment. Then I observed inelastic electron tunneling spectroscopy (IETS) for

the benzene-1,4-dithiol (BDT) molecular junctions.

Secondly, I conducted a research on BDT molecular junctions with p-doped graphene electrodes. The p-type doping of a graphene film was performed by treating pristine graphene (work function of ~4.40 eV) with trifluoromethanesulfonic (TFMS) acid, producing a significantly increased work function (~5.23 eV). From that, the enhanced charge transport properties were observed in the case of the TFMS-graphene electrode molecular junctions, as a result of a lowered charge injection barrier in the HOMO-dominating molecular junctions.

Finally, I fabricated and characterized molecular junctions consisting of diarylethene (DAE) SAMs with graphene electrodes. DAE is a photochromic molecule that forms two different conductance states, i.e., a high conductance (closed state; ON) and a low conductance (open state; OFF) state. In this research, I found unidirectional photoswitching behavior of the DAE molecular junctions and analyzed the origin of the phenomenon.

Keywords: Molecular electronics, Self-assembled monolayer, Graphene electrode, Charge transport characteristics, Interface engineering, Photoswitching molecular junction

Student Number: 2013-22993

List of Contents

List of Figures and Tables

pristine graphene and TFMS-doped graphene films. (e) Pixel-to-pixel distributions of the 2D, and G mode of the pristine graphene and TFMS-doped graphene films. (f) Hole concentration of the pristine graphene and TFMS-doped graphene films.

Figure 3.3. (a,c) Two-dimensional J-V plots of the working molecular junctions for the (a) graphene/BDT/Au and (c) TFMS-graphene/BDT/Au junctions. The inset is the average J-V curve from the measured data. (b,d) Histogram of the current density at 1 V of the working molecular junctions of the (b) graphene/BDT/Au and (d) TFMS-graphene/BDT/Au junctions.

Figure 3.4. (a,c) The representative TVS data of the (a) graphene/BDT/Au and (c) TFMS-graphene/BDT/Au junctions. (b,d) Histograms of V_T for the (b) graphene/BDT/Au and (d) TFMS-graphene/BDT/Au junctions for both voltage bias.

Figure 3.5. The representative TVS data of both positive and negative voltage regions for (a) graphene/BDT/Au junction and (b) TFMS-graphene/BDT/Au junctions.

Figure 3.6. Calculated T(E) for (a) graphene/BDT/Au, (b) TFMS-graphene/BDT/Au, and (c) Au/BDT/Au molecular junctions.

Figure 3.7. Calculated I(V) for (a) graphene/BDT/Au, (b) TFMS-graphene/BDT/Au, and (c) Au/BDT/Au molecular junctions.

Figure 3.8. Calculated FN plots for (a) graphene/BDT/Au, (b) TFMS-graphene/BDT/Au, and (c) Au/BDT/Au molecular junctions.

Figure 3.9. (a,c) The energy band diagram of the (a) graphene/BDT/Au and (c) TFMS-graphene/BDT/Au junctions at zero voltage. (b,d) The energy band diagrams of the (b) graphene/BDT/Au and (d) TFMS-graphene/BDT/Au junctions when a finite voltage below the V_T is applied. (e) The V_T versus η graphs of the graphene/BDT/Au (black symbols) and TFMS-graphene/BDT/Au junctions (red symbols) calculated based on the Landauer formula. Colored areas on the graph indicate the experimental results.

Figure 4.1. (a) Schematic representation of the fabrication process for the molecular junctions. (b) Optical (left), SEM (inset), and a cross-sectional TEM (right) image of the fabricated molecular junctions. The TEM image is superimposed with an atomic composition profile measured by EDS. (c) The chemical structures of the DAE molecule in the open (top) and closed (bottom) state.

Figure 4.2. (a) The measured optical transmittance of a MLG film on a glass substrate. (b) Raman spectra for three different areas of a MLG film. (c) A topographic profile of a MLG

film. The white scale bar in the inset image represents 4 μm.

Figure 4.3. (a) Histogram of current-density values for all open- and closed-state molecular junctions measured at a bias of V = 1 V. (b) Representative logarithmic J-V curves for the closed and open state DAE molecular junctions. (c,d) Two-dimensional logarithmic J-V plots for intact molecular junctions in (c) open and (d) closed states. Here, J_0 = 1 A/cm^2 (see the text).

Figure 4.4. (a) Real-time measurement of the current density for each state with or without exposure to light at an applied bias voltage of V = 1 V. The switching time ($t_{\text{turn-on}}$) is indicted by an arrow. (b) Histogram for the measured switching time required to transition from the open to the closed state. The Gaussian fit to the histogram is shown by the solid line, and the average switching time is shown by the dashed line.

Figure 4.5. Real-time measurement of switching from the open state to the closed state, when molecular junctions are illuminated with UV light. Set currents and extracted switching times are marked in the plots. 1 V bias was applied in all the cases.

Figure 4.6. (a,b) A representative I_{single}-V curve measured for the (a) closed and (b) open state, with the fitting curve (shown as a solid line) calculated based on the Landauer formula. The corresponding coupling and level alignment values used in the fits are listed at the bottom right of each graph. (c,d) Scatter point plots for (c) Γ and (d) E_0 values for intact molecular junctions in the closed and open state. The shaded regions represent areas, where the data points deviate by no more than 60% from the averages. Here, Γ values for the closed and open states are clearly separated from each other, while they mix for E_0. (e,f) Schematic illustration of junction structures for the (e) closed and (f) open state. The coupling strength between molecules and the electrodes Γ is indicated by the size of the arrow.

Figure 4.7. (a) Equilibrium geometry of the DAE molecule in the gas phase in its closed state, and corresponding (b) HOMO and (c) LUMO wavefunctions. (d-f) The same for the open state.

Figure 4.8. Representative I_{single}-V curves measured for the (a) closed and (b) open state of Au-DAE-rGO junctions and corresponding fitting curves. The coupling value and charge injection barrier for the I_{single}-V curves are shown at the bottom right of each graph. Scatter point plots of (c) Γ and (d) E_0 values for closed and open states of Au-DAE-rGO junctions.

Chapter 1. Introduction

1.1. Brief introduction of Molecular Electronics

Molecular electronics has been started with Aviram and Ratner with their theoretical research entitled “Molecular Rectifiers” in 1974 [1]. Modern science and technology have been developed by miniaturization, and a high density integration technology of semiconductor. However, in nanoscale, silicon based semiconductor technology is rapidly approaching its miniaturization limits due to a quantum interference effect, a quantum tunneling effect, an unstable doping problem, an overheating, etc. Seeking a new device to overcome these unavoidable limitations, molecular electronic devices are one of the most promising alternatives having extraordinary advantages compared to traditional devices [2-7]. First, countless number of degree of freedom inherent molecular structure can present numerously diverse functions including previous unavailable ones. Second, low cost of fabrication has an advantage to be industrialized in future. For the last, extremely reduced size of molecules may enable heightened capacities and faster performance.

Based on this molecular electronics, it is possible to develop a new paradigm of nano-meter scale semiconductor technology. Consequently, Molecular electronics has potential for the future of next-generation electrical circuit units. Instead of utilizing the single molecules for an active device component.

1.2. Electrical Characterization of Benzenedithiolate Molecular Junctions with Graphene Electrodes

The electrical characteristics of molecular electronic devices consisting of benzenedithiolate self-assembled monolayers and a graphene electrode have been investigated. Multilayer graphene electrode was used as a protective interlayer to prevent filamentary path formation during the evaporation of the top electrode in the vertical metal-molecule-metal junction structure [8]. The devices were fabricated both on a rigid SiO_2/Si substrate and on a flexible poly(ethylene terephthalate) (PET) substrate. Using these devices, we investigated the basic charge transport characteristics of benzenedithiolate molecular junctions in length- and temperature-dependent analyses. Additionally, the reliability of the electrical characteristics of the flexible benzenedithiolate molecular devices was investigated under various mechanical bending conditions, such as different bending radii, repeated bending cycles, and a retention test under bending. I also observed the inelastic electron tunneling spectra of our fabricated graphene-electrode molecular devices. Based on the results, we verified that benzenedithiolate molecules participate in charge transport, serving as an active tunneling barrier in solid-state graphene-electrode molecular junctions.

1.3. Interface-Engineered Charge Transport in Benzenedithiol Molecular Junctions via Chemically p-Doped Graphene Electrodes

In this study, I fabricated and characterized vertical molecular junctions consisting of self-assembled monolayers of benzenedithiol (BDT) with a p-doped multilayer graphene electrode. The p-type doping of a graphene film was performed by treating pristine graphene (work function of ~4.40 eV) with trifluoromethanesulfonic (TFMS) acid, producing a significantly increased work function (~5.23 eV) [9]. The p-doped graphene-electrode molecular junctions statistically showed an order of magnitude higher current

density and a lower charge injection barrier height than those of the pristine graphene-electrode molecular junctions, as a result of interface engineering. This enhancement is due to the increased work function of the TFMS-treated p-doped graphene electrode in the highest occupied molecular orbital-mediated tunneling molecular junctions. The validity of these results was proven by theoretical analysis based on a coherent transport model that consider asymmetric couplings at the electrode-molecule interfaces.

1.4. Unidirectional Photoswitching of Diarylethene Molecular Junctions with Graphene Electrodes

Vertical molecular junctions have been fabricated and characterized, consisting of self-assembled monolayers (SAMs) of diarylethene (DAE) contacted by a multilayer graphene (MLG) electrode on the top and gold on the bottom. The DAE molecular junctions show two stable electrical states, a closed state (high conductance) or an open state (low conductance), which are created upon illumination with UV or visible light, respectively [10-12]. For the Au-DAE-MLG junction structure, we observe that the current levels between the two conductance states are separated by two orders of magnitude. However, in a real-time measurement, we observe only unidirectional switching behavior from the open to the closed state.

References

(1) Aviram, A.; Ratner, M. A., *Chem. Phys. Lett.* **1974,** *29*, 277-283.

(2) Reed, M. A.; Zhou, C.; Muller, C. J.; Burgin, T. P.; Tour, J. M., *Science* **1997,** *278*, 252-254.

(3) Nitzan, A.; Ratner, M. A., *Science* **2003,** *300*, 1384-1389.

(4) Collier, C. P.; Wong, E. W.; Belohradský, M.; Raymo, F. M.; Stoddart, J. F.; Kuekes, P. J.; Williams, R. S.; Heath, J. R., *Science* **1999,** *285*, 391-394.

(5) Love, J. C.; Estroff, L. A.; Kriebel, J. K.; Nuzzo, R. G.; Whitesides, G. M., *Chem. Rev.* **2005,** *105*, 1103-1169.

(6) Metzger, R. M.; Chen, B.; Höpfner, U.; Lakshmikantham, M. V.; Vuillaume, D.; Kawai, T.; Wu, X.; Tachibana, H.; Hughes, T. V.; Sakurai, H.; Baldwin, J. W.; Hosch, C.; Cava, M. P.; Brehmer, L.; Ashwell, G. J., *J. Am. Chem. Soc.* **1997,** *119*, 10455-10466.

(7) Xiang, D.; Wang, X.; Jia, C.; Lee, T.; Guo, X., *Chem. Rev.* **2016,** *116*, 4318-4440.

(8) Wang, G.; Kim, Y.; Choe, M.; Kim, T. W.; Lee, T., *Adv. Mater.* **2011,** *23*, 755-760.

(9) Han, T. H.; Kwon, S. J.; Li, N.; Seo, H. K.; Xu, W.; Kim, K. S.; Lee, T. W., *Angew. Chem. Int. Ed.* **2016,** *55*, 6197-6201.

(10) Irie, M.; Kobatake, S.; Horichi, M., *Science* **2001,** *291*, 1769-1772.

(11) Whalley, A. C.; Steigerwald, M. L.; Guo, X.; Nuckolls, C., *J. Am. Chem. Soc.* **2007,** *129*, 12590-12591.

(12) Kim, D.; Jeong, H.; Lee, H.; Hwang, W. T.; Wolf, J.; Scheer, E.; Huhn, T.; Jeong, H.; Lee, T., *Adv. Mater.* **2014,** *26*, 3968-3973.

Chapter 2. Electrical Characterization of Benzenedithiolate Molecular Junctions with Graphene Electrodes

2.1. Introduction

Molecular electronics, in which single molecules or molecular monolayers are used as active components of electronic devices, has been widely studied as the ultimate miniaturization of electronic devices [1-10]. Various attempts have been made to produce molecular junctions for the purpose of investigating the characteristics of charge transport in the molecular regime, using approaches such as mechanically controllable break junctions (MCBJs), electromigrated nanogap fabrication, scanning probe microscopy, the fabrication of eutectic gallium–indium (EGaIn) junctions, and various solid-state device fabrication methods [2, 9, 11-17]. In particular, vertical-type solid-state devices based on an evaporated metal-molecule-metal junction structure have received significant attention as a general test-bed platform for investigating the charge transport characteristics of molecular junctions. However, the direct metal evaporation process used to form the top electrode can easily create electrical shorts via the formation of filamentary paths through the molecules, which results in junctions that are unsuitable for characterization [18-24]. To solve this problem, various approaches have been proposed, for example, introducing an interlayer between the top metal electrode and molecular layers conducting polymer poly(3,4-ethylenedioxythiophene) polystyrene sulfonate (PEDOT:PSS), multilayer graphene (MLG), or reduced graphene oxide (rGO) [25-34]. In addition, novel fabrication

techniques in which the top electrode can be produced without causing damage to the molecular layer, such as direct transfer methods, have been proposed [35, 36]. The ultimate aim of these various approaches is to improve the reliability of molecular electronic devices. Among these methods, MLG-interlayer-based molecular junctions in particular offer various advantages by virtue of their graphene electrodes. Graphene is a two-dimensional sheet of carbon atoms with excellent electronic properties [37, 38]. It can be synthesized as large-area, flexible, and conductive films that are suitable for use as electrodes [39, 40]. Using such graphene films as interlayer electrodes in molecular junctions, a previous study demonstrated a high device yield and stability over a long period, accompanied by the capability of mass production, nontoxicity, and low contact resistance comparable to that of pure metal-molecule-metal junctions [29]. However, to date, only one kind of molecule (i.e., alkanethiolate) has been studied as a test-bed molecule for this type of molecular junction. In addition, the fabrication of graphene-interlayer molecular junctions on flexible substrates has not yet been demonstrated. It has only been demonstrated that molecular devices with a conducting polymer (PEDOT:PSS) interlayer can be fabricated using various kinds of molecules (alkanethiolates, diodes, and photoswitching molecules) on flexible substrates [26-28, 31, 34]. Furthermore, the inelastic electron tunneling spectroscopy (IETS) characteristics of graphene-interlayer molecular junctions has not yet been verified. Therefore, extending our understanding of graphene-interlayer molecular electronic devices is a great necessity.

In this study, we report the electrical characteristics of molecular electronic devices fabricated from benzenedithiolate self-assembled monolayers (SAMs), both on a rigid SiO_2/Si substrate and on a flexible poly(ethylene terephthalate) substrate. We used an MLG electrode as a protective interlayer to prevent electrical shorts in the vertical molecular

junction structure. We investigated the fundamental charge transport characteristics of the benzenedithiolate molecular junctions. In particular, the reliability of the electrical characteristics of the flexible molecular devices was studied under various mechanical bending conditions. Inelastic electron tunneling spectra of the graphene-interlayer benzenedithiolate molecular devices were also characterized.

2.2. Experiments

2.2.1. Device fabrication process

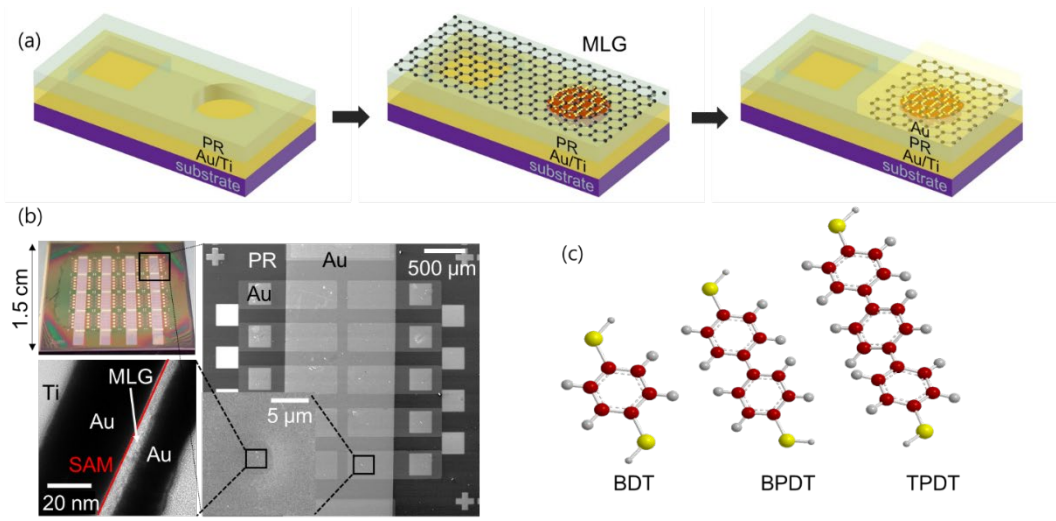

Figure 2.1 (a) Schematic illustration of the device fabrication process for the graphene-interlayer-electrode molecular junctions. Left: bottom electrode deposition and photoresist wall formation. Middle: SAM deposition and MLG transfer. Right: top electrode deposition and molecular device completion. (b) Optical, SEM, and TEM images of the molecular devices. (c) The three types of molecules with their chemical structures: BDT, BPDT, and TPDT.

Figure 2.1 shows a schematic illustration of the device fabrication process for our graphene-interlayer molecular junctions. We followed the same junction fabrication process that we have previously reported [19, 28, 29, 35]. In brief, the bottom electrodes (30 nm Au/5 nm Ti) were first patterned via a shadow mask using an electron beam evaporator operating at a rate of 0.2 Å/s on a p-type (100) SiO_2/Si (300 nm) or a flexible poly(ethylene terephthalate) (PET) substrate. Then, optical lithography was used to create 2 μm radius holes through walls of photoresist (AZ5214E from AZ Electronic Materials). Each sample was immersed for 3 hours in a 5 mM molecular solution diluted with ethanol in a N_2-filled glove box, causing SAMs to form on the exposed Au surfaces. For this study, we chose three different benzenedithiolate molecules: benzene-1,4-dithiol (BDT), biphenyl-4,4'-dithiol (BPDT), and p-terphenyl-4,4''-dithiol (TPDT). After the SAM deposition, an MLG film was transferred to cover the surface of each sample using the direct metal transfer (DMT) method, as we have previously reported [35]. To produce the MLG interlayer, an MLG film was first grown in a chemical vapor deposition (CVD) chamber on a Ni (300 nm) / Ti (10 nm) / Si substrate (under a gas flow of 15 sccm CH_4 and 20 sccm Ar/H_2 at 20 Torr for 10 min at 900 ºC). After growth was complete, a layer of poly(methylmethacrylate) (PMMA, 950PMMA A5 from MicroChem Corp.) was spin coated onto the film as a dummy layer, and support tape was attached to the PMMA. Then, the Ni of the substrate was etched using an iron(III) chloride ($FeCl_3$) aqueous solution. The MLG film was then placed onto the molecular layer to make contact through the van der Waals interaction. Afterward, a few drops of isopropyl alcohol (IPA) were applied to the molecular layer to form a fine contact via the surface tension of the IPA solution during its vaporization [41]. Then, the sample was dried for ~12 h, and the PMMA was removed with acetone. The top electrode was deposited in the same way as the bottom electrode (15 nm

thick Au), using the same patterned shadow mask, with the evaporator operating at a rate of 0.1 Å/s. Finally, the remaining MLG film was removed by means of an oxygen plasma treatment under 10 sccm of O_2 gas at 50 W of forward power to prevent the formation of any direct pathway though the top and bottom electrodes. Detailed schematic of fabrication procedure is given in Figure 2.2.

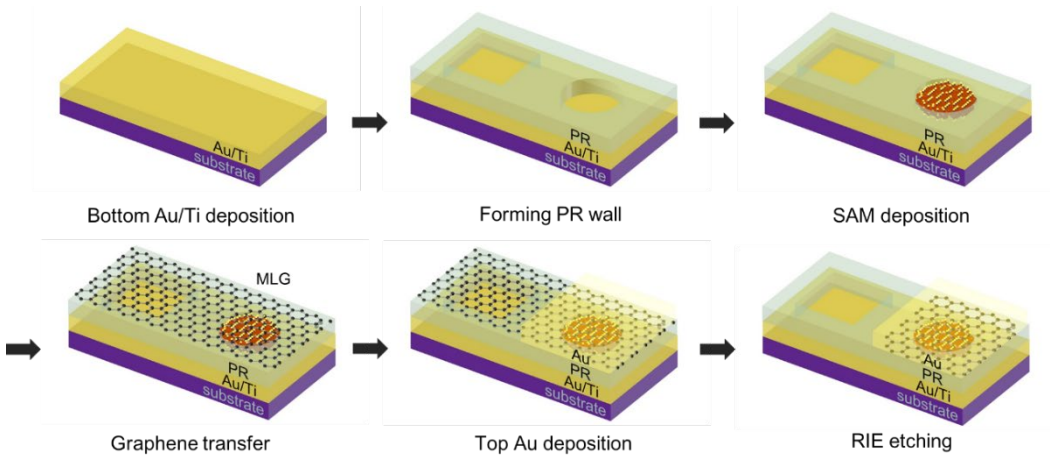

Figure 2.2. Device fabrication procedure.

2.2.2 IETS measurement setup

IETS measurements were performed at 4.2 K using a custom-made cryogenic vacuum chamber in which BDT molecular devices were mounted inside a liquid He dewar. Each device was placed on a 16-pin IC chip carrier socket and then electrically shielded inside the vacuum chamber. The detailed circuit diagram of the IETS setup is provided in Figure 2.4b. The current was measured using a digital multimeter (Agilent 34410) with a 16-bit digital-to-analog converter (DAC) as a DC source and a low-noise current amplifier (Ithaco 1211). The first (dI/dV) and second (d^2I/dV^2) derivatives of the current with respect to the voltage were measured following the standard AC modulation technique using a lock-in amplifier (LIA, Stanford Research Systems SR830). The root-mean-square (rms) AC modulation bias was 5 mV at a frequency of 503 Hz. The reference phase was -90 degrees when the second harmonic was measured for d^2I/dV^2 (there was no phase shift for the first harmonic). Finally, the DC voltage was swept from 0 to 0.3 V.

2.2.3 Electrical characterization

The electrical characteristics of the device were measured using a semiconductor parameter analyzer (HP 4145B) in a probe station (JANIS Model ST-500). Between each measurement.

2.3. Results and Discussions

2.3.1. Electrical characteristics of benzenedithiolate molecular devices

Although alkanethiolates are a common choice for molecular junction test-beds, benzene-based conjugate molecules are also important because their conjugate electronic structure can induce interesting electrical behaviors with various advantages [42-44]. We chose three types of benzenedithiolates because they are the simplest and most widely studied conjugate molecules in the field of molecular electronics and also one of the most promising families of prototype molecules for studying the fundamentals of charge transport. Choosing benzenedithiolate molecules allowed us to compare the data measured from our fabricated MLG-interlayer molecular devices with those from benzenedithiolate molecular junctions fabricated using other known methods. Various studies have indicated that the primary mechanism of charge transport through benzenedithiolate is non-resonant tunneling (when the applied voltage is not too high), in which the current density exhibits an exponential dependence on the molecular length, as in the case of alkanethiolates [45-48]. However, because conjugate molecules have far smaller gaps between the highest occupied molecular orbital (HOMO) and the lowest unoccupied molecular orbital (LUMO) than do saturated molecules such as alkanethiolates, higher conductance is expected. By replacing BDT with BPDT and TPDT (thereby increasing the number of phenyl rings), we could measure the decay coefficient (β) per phenyl ring and compare this β value with previously reported values [45-49]. Figure 2.3a shows the statistically derived current density-voltage (J-V) characteristics on a logarithmic scale for all working BDT, BPDT, and TPDT molecular devices with graphene electrodes on the rigid SiO_2/Si substrate.

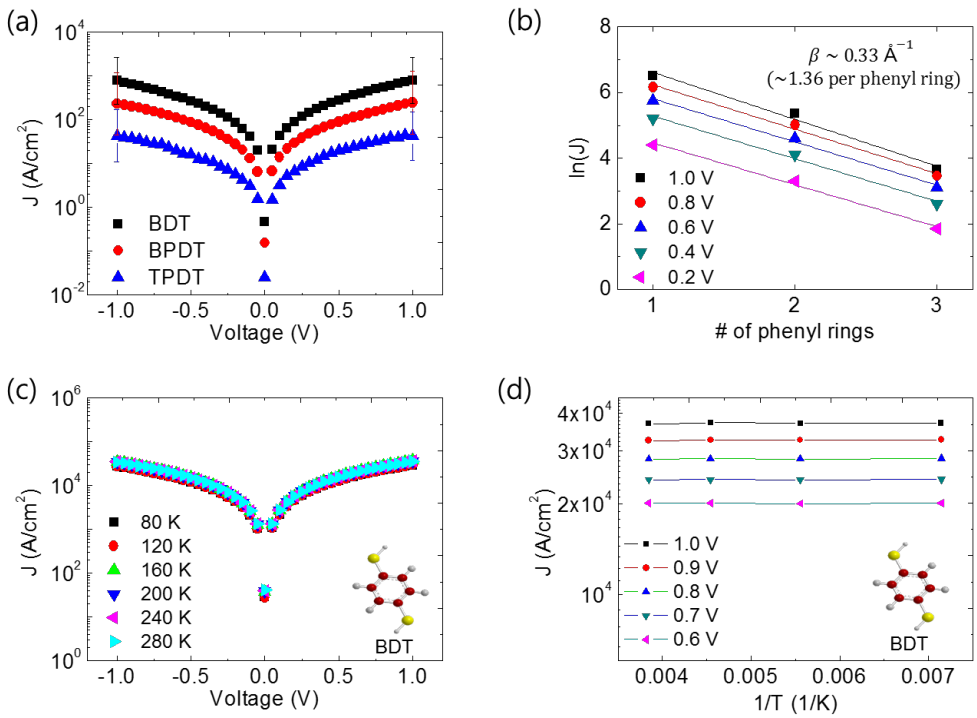

Figure 2.3. (a) Statistically derived J-V characteristics of all working BDT, BPDT, and TPDT molecular devices with graphene electrodes. (b) A semi-log plot of the J values at different biases versus the numbers of phenyl rings in the BDT, BPDT, and TPDT molecular devices. (c) Semi-log plot of the current densities measured at different biases from 0.2 to 1 V as a function of the molecular length. This graph shows an exponential decrease in the current density as the molecular length increases. (c) J-V-T measurements of a BDT molecular device. The temperature was varied from 80 to 280 K in increments of 40 K. (d) Arrhenius plot of the J-V-T measurements of the BDT device, presented to verify the type of charge transport occurring in the device.

We fabricated a sufficient number of devices to conduct a statistical analysis for each type of molecular junction, and we identified the operating devices by fitting the histograms based on a Gaussian distribution function. The range of operation for the devices was determined to extend from $\mu - \sigma$ to $\mu + \sigma$, where μ is the Gaussian average of the current density (in units of A/cm^2) at 1 V and σ is the Gaussian standard deviation. The error bars marked at ± 1 V represent the standard deviations of the operating devices. From the operating devices, the log-averaged current densities (J) at 1 V for BDT, BPDT, and TPDT were found to be 2.90 A/cm^2, 2.39 A/cm^2, and 1.62 A/cm^2, respectively. These results indicate that the current density decreases with an increasing number of phenyl rings. Note that the difference per ring is smaller than that observed in the case of alkanethiolate molecular junctions because benzenedithiolate molecules form a smaller tunneling barrier than do alkanethiolates, i.e., benzenedithiolate molecules exhibit a smaller tunneling decay coefficient (β). Figure 2.3b presents a semi-log plot of the J values at different biases, from 0.2 to 1 V, versus the numbers of phenyl rings in the molecules of the BDT, BPDT, and TPDT devices. This graph shows an exponential decrease in the current density as the molecular length increases. Based on the non-resonant tunneling model ($J = J_0 e^{-\beta d}$, where β is the decay coefficient and d is the molecular length), we could determine β by performing a linear fit for each bias. The average β value was found to be 0.33 ± 0.02 Å^{-1} [1] (1.36 ± 0.06 per phenyl ring), in good agreement with previously reported values [45-48]. To determine the characteristics of the tunneling transport through our molecular junctions, we performed a temperature-varying current density-voltage (J-V-T) analysis to identify the temperature dependence of the J-V characteristics. Figure 2.3c depicts the J-V-T measurements of the BDT molecular devices. The temperature was varied from 80 to 280 K in increments of 40 K. Figure 2.3d, which represents an alternate means of plotting the

dataset presented in figure 2.3c, shows the Arrhenius plot (J versus 1/T) to verify the type of charge transport occurring in the device. This graph shows the temperature-independent characteristics of the current density, which imply that the primary mechanism of charge transport in our molecular junctions is indeed non-resonant tunneling; this is consistent with the results of previous studies [47, 48].

2.3.2. Bending characteristics of flexible molecular devices

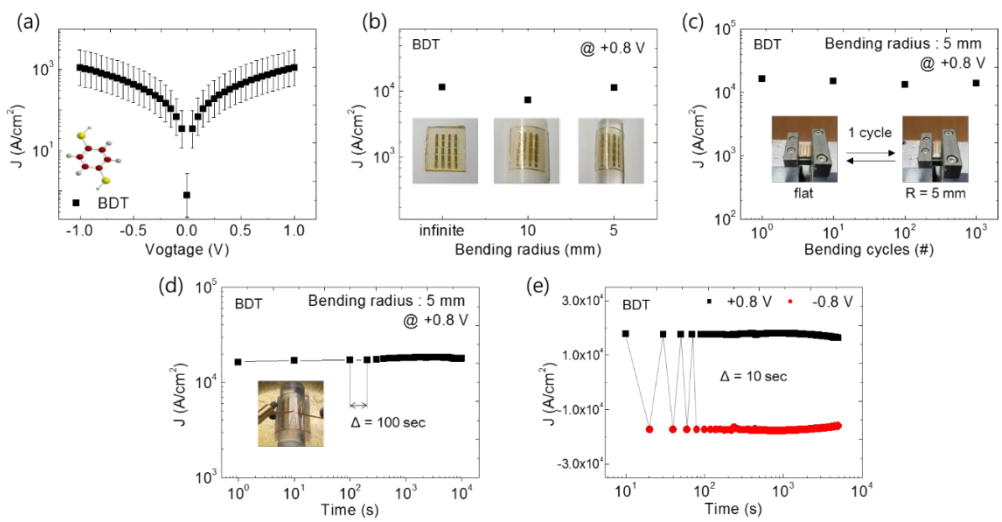

Figure 2.4. (a) J-V curve for the BDT molecular devices on the flexible substrate under flat conditions (bending radius = ∞). (b) Current densities measured at 0.8 V in different bending configurations (bending radii of ∞, 10 mm, and 5 mm). (c) J-V characteristics measured throughout 10^3 bending cycles of repeated 5 mm radius bending using a bending machine. (d) Retention characteristics of a molecular device with a 5 mm bending radius. A voltage of 0.8 V was applied in intervals of a duration that was increased in increments of 100 s up to 10^4 s. (e) Retention characteristics with voltage switching between +0.8 and -0.8 V at intervals of 10 s, where the current persisted up to 5000 s.

We also fabricated the same BDT molecular devices with MLG electrodes on a flexible PET substrate. PET is attractive for use as a substrate for molecular junctions because it offers various advantages such as outstanding durability, thermal stability, and weatherproofness [50, 51]. Moreover, PET is insoluble by organic solvents such as ethanol and acetone. Because our device fabrication process entails several steps of solution processing (SAM deposition in an ethanol solution and PMMA removal in acetone), a PET substrate is a suitable choice for the fabrication of our molecular devices. Figure 2.4(a) shows the J-V curve for the BDT molecular devices on the PET flexible substrate under flat conditions (bending radius = ∞). This graph shows that the order of the current density is the same as that for the devices fabricated on the rigid substrate. The reliability of the electrical characteristics of the flexible molecular devices was also examined under various bending conditions. Figure 2.4b presents the current densities measured at 0.8 V under different bending configurations (bending radii of ∞, 10 mm, and 5 mm). The current density remained nearly constant regardless of the bending radius. This result demonstrates that the electrical characteristics of our molecular devices do not degrade under mechanical distortion. Figure 2.4c shows the J-V characteristics measured throughout 10^3 bending cycles of repeated 5 mm radius bending using a bending machine (see the inset of figure 2.4c). This result confirms the endurance of our devices under continuous, repeated mechanical stress. We also performed a retention test with a 5 mm bending radius, as shown in figure 2.4d. A voltage of 0.8 V was applied for intervals of a duration that was increased in increments of 100 s. Under these conditions, the currents were maintained for up to 10^4 s. Figure 2.4e shows the result of a similar measurement conducted with voltage switching between +0.8 and -0.8 V at intervals of increasing duration in increments of 10 s, in which the currents were again well maintained for up to 5000 s. Based on these results, we can

confirm that the electrical characteristics of our molecular devices with MLG electrodes are well preserved regardless of mechanical stress.

2.3.3. Inelastic Electron Tunneling Spectroscopy (IETS) Measurements

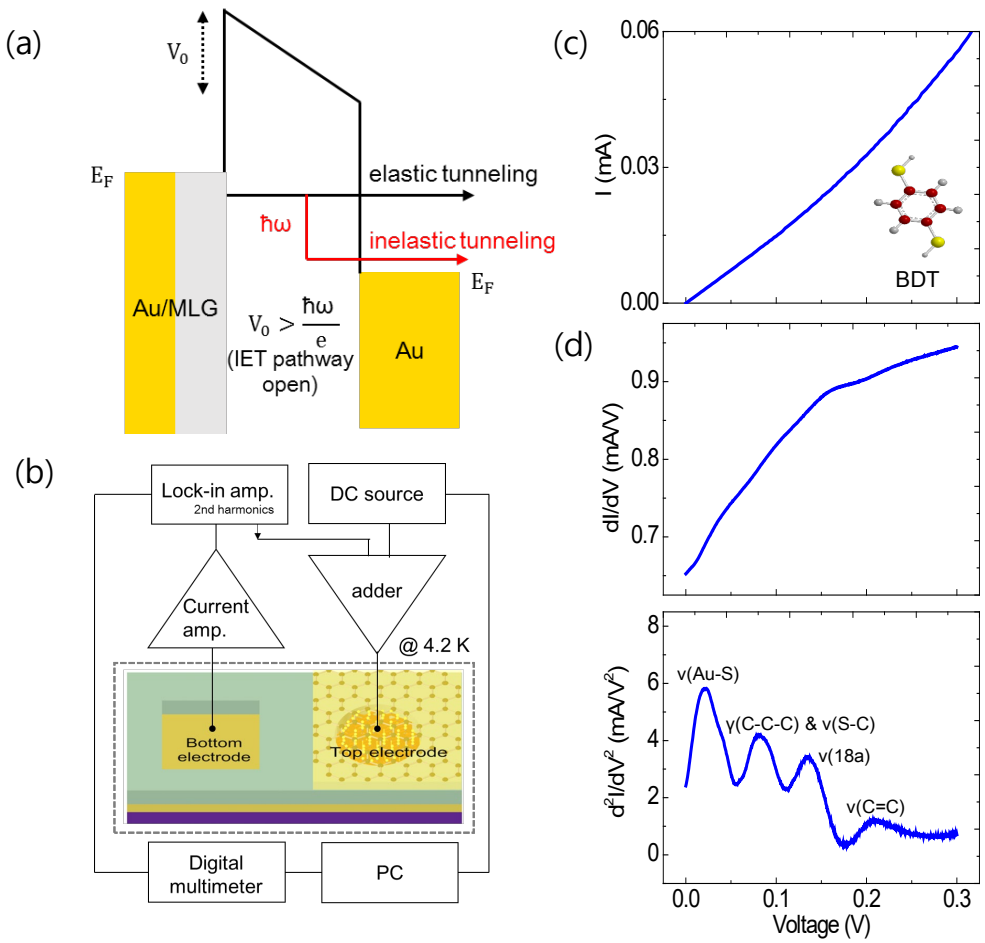

Figure 2.5. (a) Energy band diagram describing the principles of IETS. The black arrow represents elastic tunneling, and the red arrow represents transmission through the molecule via an inelastic tunneling process. The inelastic channel is available only when the bias voltage V_0 exceeds the specific phonon energy ħω/e. (b) Circuit diagram of our IETS setup. (c) I(V), dI/dV, and d^2I/dV^2 plots of a BDT molecular device with a graphene electrode. In the d^2I/dV^2 plot, IETS peaks can be observed at 21, 82, 136, and 209 mV.

In addition to fundamental current-voltage characterization and temperature-varying measurements, various techniques are available for investigating the charge transport characteristics of molecular junctions, including transition voltage spectroscopy (TVS), noise spectroscopy, thermoelectric measurements, surface-enhanced Raman spectroscopy (SERS), and IETS [52-56]. IETS in particular has been proposed as a powerful tool for the detection of unique vibration modes of molecules in a tunneling junction. Several studies have been performed concerning IETS measurements of alkanethiolate SAMs in nanopore structures, single alkanethiolate or BDT molecules in MCBJs, and electromigrated nanogap junctions, as well as the use of scanning tunnel microscope (STM) techniques [48, 57-60]. Recently, we reported the results of IETS measurements of pure metal-molecule-metal solid-state junctions fabricated using a direct transfer method [36]. However, the IETS characteristics of graphene-interlayer molecular devices have not yet been verified. Thus, we studied the IETS spectra of our BDT molecular junctions with MLG electrodes, which were found to be consistent with previously reported theoretical and experimental results [48, 59-66]. From this, we ascertained that IETS signals can be successfully observed in graphene-interlayer molecular junctions and confirmed the molecular signatures in these junctions. The principles of IETS have previously been explained in the literature [61, 62]. Here, we will briefly reiterate them. When a negative voltage is applied to an Au/MLG electrode, its Fermi level is raised (figure 2.5a). Then, an electron on the Au/MLG electrode begins to tunnel into the empty states of the right-hand Au electrode through an energy-conserving process known as elastic tunneling (black arrow). Alternatively, the electron can also tunnel through the junction with an energy loss by delivering an energy quantum, $\hbar\omega$, into a localized vibrational mode of the molecule. This energy is used to excite the molecule's vibrational mode. The electron

is eventually transmitted through the molecule through an inelastic tunneling process (red arrow). The inelastic channel is available only if the bias V_0 exceeds the specific phonon energy ħω/e. When only the elastic tunneling channel is open, the current will increase linearly with an increase in voltage. However, when the inelastic channel becomes available at the threshold voltage ($V_0 = ħω/e$), this effect creates a small shunt in the slope of the I-V curve. In the conductance (dI/dV-V) graph, a step is formed at V_0. At the same time, a peak appears in the second derivative (d^2I/dV^2-V) graph, namely, an IETS peak. Multiple peaks can be observed if multiple molecular vibrational modes exist; therefore, analyzing the positions of the IETS peaks informs us of the intrinsic vibrational characteristics of the molecule(s) in a junction. Figure 2.5b presents the circuit diagram of our IETS setup. Because the inelastic tunneling current is a very small portion of the overall tunneling current, it is necessary to use an AC modulation technique with LIAs to directly identify the second derivative of the current. We measured the first and second harmonic signals, which are proportional to dI/dV and d^2I/dV^2, respectively; then, after adjusting parameters such as the LIA amplitude, LIA sensitivity, current amplifier sensitivity, and transformer factor, we identified the exact dI/dV and d^2I/dV^2 values. Additionally, the IETS measurements were performed at 4.2 K to prevent thermal broadening of the signals. Figure 2.5c shows the I(V), dI/dV, and d^2I/dV^2 plots of our BDT molecular devices with MLG electrodes. The current measurements were performed from 0 to 0.3 V. The current-voltage (I-V) graph appears as a smooth curve without any kinks. This shape indicates that the contribution from inelastic tunneling is far smaller than the elastic tunneling current, causing the slope shunts in the I-V graph to be barely noticeable. However, the conductance (dI/dV) curve abruptly increases at certain specific voltages. The shape of this graph shows clear evidence of inelastic tunneling. In the d^2I/dV^2 plot, an obvious inelastic tunneling

phenomenon is evident. Several peaks are apparent at 21, 82, 136, and 209 mV, namely, the IETS peaks. The first peak, at 21 mV, is the ν(Au-S) peak, which corresponds to a strong stretching energy between the thiol end groups and the Au atoms in the bottom electrode [48,59-66]. The other three peaks originate from the intrinsic vibrational modes of the phenyl ring. The second peak, at 82 mV, is expected to arise from the C-C-C in-plane bending mode γ(C-C-C) and the S-C stretching mode ν(S-C) [48, 59-66]. The third and fourth peaks, at 136 and 209 mV, originate from the ν(18a) C-H in-plane stretching and ν(C=C) stretching modes [48, 59-66]. Our experimental results are well consistent with various previous IETS theories and experiments regarding Au-BDT-Au single-molecule junctions [48, 59, 60, 64, 66]. As a result, the role of the BDT molecule as an active transport channel in our molecular device was confirmed by this IETS experiment. One interesting feature is that the intensity of the peaks decreases in the following order: ν(Au-S) > γ(C-C-C) & ν(S-C) > ν(18a) > ν(C=C). This means that electron tunneling through the Au-S bond is the most favorable inelastic pathway in this junction. Lin *et al.* theoretically suggested that the origin of the intensity ordering of the IETS peaks of an Au-BDT-Au junction is the rotation of the BDT molecule around its S-S axis and that this rotational freedom permits variations in the intensity of each peak [64, 66]. The other noticeable feature is that no clear trace of the graphene electrode is observed in the IETS signals even though MLG exhibits a strong Raman shift peak at approximately 1580 cm^{-1} (196 mV) [67]. Moreover, many other IETS peaks of graphene have also been reported recently [68-71]. However, in this study, we observed only the molecular peaks. This finding implies that the graphene electrode in this metal-molecule-graphene system yields only weak signals and that the weak graphene peaks were overlapped with stronger molecular excitations.

However, further theoretical and experimental studies of the electron-phonon interactions in molecular junctions with graphene electrodes will certainly be necessary in the future.

2.4. Conclusion

In summary, we investigated the electrical characteristics of benzenedithiolate molecular electronic devices with graphene electrodes. The devices were fabricated on both rigid and flexible substrates. We investigated the basic properties of tunneling transport in these devices through current-voltage, molecular-length-dependent, and temperature-dependent characterizations. Additionally, we examined the reliability of the molecular devices fabricated on flexible substrates under various mechanical bending conditions. The electrical characteristics of the devices were well maintained in all tested bending environments. Finally, we observed the IETS peaks of the fabricated graphene-interlayer molecular junctions and demonstrated the role of the benzenedithiolate molecule as an active tunneling component in these molecular junctions. This study extends our understanding of the electrical characteristics of conjugate molecular junctions with graphene electrodes and may thus contribute to the development of reliable device fabrication platforms and future applications of molecular electronics.

References

(1) Aviram, A; Ratner, M. A., *Chem. Phys. Lett.* **1974,** *29*, 277.

(2) Reed, M. A.; Zhou, C.; Muller, C. J.; Burgin, T. P.; Tour, J. M., *Science* **1997**, *278,* 252.

(3) Chen, J.; Reed, M. A.; Rawlett, A. M.; Tour, J. M., *Science* **1999,** *286* (5444), 1550-1552.

(4) Nitzan, A; Ratner, M. A., *Science* **2003,** *300,* 1384.

(5) Matsuda, K; Irie, M., *J. Am. Chem. Soc.* **2001,** *123*, 9896.

(6) Galperin, M; Ratner, M. A.; Nitzan, A.; Troisi, A., *Science* **2008,** *319*, 1056.

(7) Love, J. C.; Estroff, L. A.; Kriebel, J. K.; Nuzzo, R. G.; Whitesides, G. M., *Chem. Rev.* **2005,** *105,* 1103.

(8) Nijhuis, C. A.; Reus, W. F.; Siegel, A. C.; Whitesides, G. M., *J. Am. Chem. Soc.* **2011**, *133* 15397.

(10) Behin-Aein, B; Datta, D; Salahuddin, S; Datta, S., *Nat. Nanotechnol.* **2010,** *5*, 266.

(11) Zhou, C.; Muller, C. J.; Deshpande, M. R.; Sleight, J. W.; Reed, M. A., *Appl.Phys.Lett.* **1995,** *67*, 1160.

(12) Park, H.; Lim, A. K. L.; Alvisatos, A. P.; Park, J.; McEuen, P. L., *Appl. Phys. Lett.* **1999,** *75*, 301.

(13) Strachan, D. R.; Smith, D. E.; Johnston, D. E.; Park, T. H.; Therien, M. J.; Bonnell, D. A.; Johnson, A. T., *Appl. Phys. Lett.* **2005,** *86*, 043109

(14) Poirier, G. E., *Chem. rev.* **1997**, *97*, 4.

(15) Datta, S.; Tian, W.; Hong, S.; Reifenberger, R.; Henderson, J. I.; Kubiak, C. P., *Phys. Rev. Lett.* **1997**, *79* 13.

(16) Simeone, F. C.; Yoon, H. J.; Thuo, M. M.; Barer, J. R.; Smith, B.; Whitesides, G. M., *J. Am. Chem. Soc.* **2013,** *135*, 18131.

(17) Nijhuis, C. A.; Reus, W. F.; Barber, J. R.; Whitesides, G. M., *J. Phys. Chem. C* **2012,** *116*, 14139.

(18) Haick, H.; Cahen, D., *Accounts Chem. Res.* **2008,** *41*, 359.

(19) Kim, T.-W.; Wang, G.; Lee, H.; Lee, T., *Nanotechnology* **2007,** *18*, 315204

(20) de Boer, B.; Frank, M. M.; Chabal, Y. J.; Jiang, W. R.; Garfunkel, E.; Bao, Z., *Langmuir* **2004,** *20*, 1539.

(21) Haick, H.; Niitsoo, O.; Ghabboun, J.; Cahen, D., *J. Phys. Chem. C* **2007,** *111*, 2318.

(22) Walker, A. V.; Tighe, T. B.; Cabarcos, O. M.; Reinard, M. D.; Haynie, B. C.; Uppili, S.; Winograd, N.; Allara, D. L., *J. Am. Chem. Soc.* **2004,** *126,* 3954.

(23) Wang, G.; Kim, T.-W.; Lee, H.; Lee, T., *Phys. Rev. B* **2007,** *76*, 205320.

(24) Lau, C. N.; Stewart, D. R.; Williams, R. S.; Bockrath, M., *Nano. Lett.* **2004,** *4*, 4.

(25)Akkerman, H. B.; Blom, P. W. M.; de Leeuw, D. M.; de Boer, B., *Nature* **2006,** *441*, 69.

(26) Jeong, H.; Kim, D.; Wang, G.; Park, S.; Lee, H.; Cho, K.; Hwang, W. T.; Yoon, M. H.; Jang. Y. H.; Song, H.; Xiang, D.; Lee, T., *Adv. Funct. Mater.* **2014,** *24*, 2472.

(27) Kim, D.; Jeong, H.; Lee, H.; Hwang, W T.; Wolf, J.; Scheer, E.; Huhn, T.; Jeong, H.; Lee, T., *Adv. Mater.* **2014**, *26*, 2968

(28) Park, S.; Wang, G.; Cho, B.; Kim, Y.; Song, S.; Ji, Y.; Yoon, M. –H.; Lee, T., *Nat. Nanotechnol.* **2012,** *7*, 438.

(29) Wang, G.; Kim, Y.; Choe, M.; Kim, T. –W.; Lee, T., *Adv. Mater.* **2011,** *23*, 755.

(30) Li, T.; Hauptmann, J. R.; Wei, Z.; Petersen, S.; Bovet, N.; Vosch, T.; Nygård, J.; Hu, W.; Liu, Y.; Bjφrnhom, T.; Nφrgaard, K.; Laursen, B. W., *Adv. Mater.* **2012,** *24*, 1333.

(31) Seo, S.; Min, M.; Lee, S. M.; Lee, H., *Nat. Commun.* **2013,** *4,* 1920.

(32) Seo, S.; Min, M.; Lee, J.; Lee, T.; Choi, S. –Y.; Lee, H., *Angew. Chem. Int. Edit.* **2012,** *51*, 108.

(33) Li, T.; Hauptmann, J. R.; Wei, Z.; Petersen, S.; Bovet, N.; Vosch, T.; Nygard, J.; Hu, W.; Liu, Y.; Bjornholm, T.; Norgaard, K.; Laursen, B. W., *Adv. Mater.* **2012**, *24*, 1333.

(34) Kim, D.; Jeong, H.; Hwang, W. T.; Jang, Y.; Sysoiev, D.; Scheer, E.; Huhn, T.; Min, M.; Lee, H.; Lee, T., *Adv. Funct. Mater.* **2015,** *25*, 5918.

(35) Jeong, H.; Kim, D.; Kim, P.; Cho, M. R.; Hwang, W. T.; Jang, Y.; Cho, K.; Min, M.; Xiang, D.; Park, Y, D.; Jeong, H.; Lee, T., *Nanotechnology* **2015,** *26*, 025601.

(36) Jeong, H.; Hwang, W. T.; Kim, P.; Kim, D.; Jang, Y.; Min, M.; Xiang, D.; Song, H.; Park, Y. D.; Jeong, H.; Lee, T., *Appl. Phys. Lett.* **2015,** *106,* 063110.

(37) Novoselov, K. S.; Geim, A. K.; Morozot, S. V.; Jiang, D.; Zhang, Y.; Dubonos, S. V.; Grigorieva, I. V.; Firsov, A. A., *Science* **2004**, *306*, 666.

(38) Wang, Q. H.; Hersam, M. C., *Nat. Chem.* **2009,** *1,* 206.

(39) Kim, K. S.; Zhao, Y.; Jang, H.; Lee, S. Y.; Kim, J. M.; Kim, K. S.; Ahn, J. G.; Kim, P.; Choi, J. Y.; Hong, B. H., *Nature* **2009,** *457*, 706.

(40) Reina, A.; Jia, X.; Ho, J.; Nezich, D.; Son, H.; Bulovic, V.; Dresselhaus, M. S.; Kong, J., *Nano. Lett.* **2008,** *9*, 30.

(41) Regan, W.; Alem, N.; Aleman, B.; Geng, B.; Grit, C.; Maserati, L.; Wang, F.; Crommie, M.; Zettl, A., *Appl. Phys. Lett.* **2010,** *96*, 113102.

(42) Weiss, E. A.; Wasielewski, M. R.; Ratner, M. A., *Top. Curr. Chem.* **2005,** *57*, 103.

(43) Ng, M. K.; Yu, L., *Angew. Chem. Int. Edn* **2002**, *41*, 3598.

(44) Collier, C. P.; Wong, E. W.; Belohradsky, M.; Raymo, F. M.; Stoddart, J. F.; Kuekes, P. J.; Williams, R. S.; Heath, J. R., *Science* **1999**, *285*, 391.

(45) Tao, N. J., *Nat. Nanotechnol.* **2006**, *1*, 173.

(46) Choi, S. H.; Kim, B.; Frisbie, C. D., *Science* **2008,** *320*, 1482.

(47) Wold, D. J.; Haag, R.; Rampi, M. A.; Frisbie, C. D., *J. Phys. Chem. B* **2002,** *106*, 2813.

(48) Song, H.; Kim, Y.; Jeong, H.; Reed, M. A.; Lee, T., *J. Appl. Phys* **2011,** *109,* 102419.

(49) Holmlin, R. E.; Haag, R.; Chabinyc, M. L.; Ismagilov, R. F.; Cohen, A. E.; Terfort, A.; Rampi, M. A.; Whitesides, G. M., *J. Am. Chem. Soc.* **2001,** *123*, 5075.
(50) Jeziomy, A., *Polymer* **1978,** *9*, 10.
(51) Holdsworth, P. J.; Turner-Jones, A., *Polymer* **1971,** *12*, 3.
(52) Beebe, J. M.; Kim, B.; Gadzuk, J. W.; Frisbie, C. D.; Kushmerick, J. G., *Phys. Rev. Lett.* **2006,** *97,* 026801.
(53) Nie, S.; Emory, S. R., *Science* **1997,** *275,* 5303.
(54) Kim, Y.; Song, H.; Strigl, F.; Pernau, H. F.; Lee, T.; Scheer, E., *Phys Rev. Lett.* **2011,** *106*, 196804.
(55) Reddy, P.; Jang, S. Y.; Segalman, R. A.; Majumdar, A., *Science* **2007,** *315*, 1568.
(56) Jaklevic, R. C.; Lambe, J., *Phys. Rev. Lett.* **1966**, *17*, 1139.
(57) Okabayashi, N.; Konda, Y.; Komeda, T., *Phys. Rev. Lett.* **2008,** *100*, 217801.
(58) Wang, W.; Lee, T.; Kretzschmar, I.; Reed, M. A., *Nano Lett.* **2004,** *4*, 4.
(59) Kim, Y.; Pietsch, T.; Erbe, A.; Belzig W,.; Scheer, E., *Nano Lett.* **2011,** *11,* 3734.
(60) Song, H.; Kim, Y.; Jang, Y. H.; Jeong, H.; Reed, M. A.; Lee, T., *Nature* **2009**, *462*, 1039.
(61) Hansma, P. K., *Phys. Lett. C Phys. Rep* **1977,** *30*, 145.
(62) Adkins, C. J.; Phillips, W. A.; *J. Phys. C* **1985,** *18*, 1313.
(63) Taniguchi, M.; Tsutsui, M.; Yokota, K.; Kawai, T., *Nanotechnology* **2009,** *20*, 434008.
(64) Lin, L. L.; Wang, C. K.; Luo, Y., *ACS Nano* **2011,** *5*, 2257.
(65) Kula, M.; Luo, Y., *J. Chem. Phys.* **2008,** *128*, 064705.
(66) Lin, L. L.; Jiang, J.; Luo, Y., *Physica E* **2013,** *47*, 167.
(67) Ferrari, A. C.; Meyer, J. C.; Scardaci, V.; Casiraghi C.; Lazzeri, M.; Mauri, F.; Piscanec S.; Jiang, D.; Novoselov, K. S.; Roth, S.; and Geim, A. K., *Phys. Rev. Lett.* **2006,** *97*, 187401.
(68) Zhang, Y.; Brar, V. W.; Wang, F.; Girit, C.; Yayon, Y.; Panlasigui, M.; Zettl, A.; Crommie, M. F., *Nat. Phys.* **2008,** *4*, 627.
(69) Natterer, F. D.; Wyrick, J.; Chan, Y. H.; Ruan, W. Y.; Chou, M. Y.; Watanabe, K.; Taniguchi, T.; Zhitenev, N. B.; Stroscio, J. A., *Phys. Rev. Lett.* **2015,** *114,* 245502.
(70) Brar, V. W.; Wickenburg, S.; Panlasigui, M.; Park, C. H.; Wehling, T. O.; Zhang, Y.; Decker, R.; Girit, C.; Balatsky, A. V.; Louie, S. G.; Zettl, A.; Crommie, M. F., *Phys. Rev. Lett.* **2010**, *104*, 036805.
(71) Castellanos-Gomez, A.; Rubio-Bollinger, G.; Barja, S.; Garnica, M.; de Parga, A. L. V.; Miranda, R.; Agrait, N., *Appl. Phys. Lett.* **2013,** *104*, 036805.

Chapter 3. Interface-Engineered Charge Transport Properties in Benzenedithol Molecular Electronic Junctions via Chemically p-doped Graphene Electrodes

3.1. Introduction

In molecular-scale electronic junctions, the interface of the electrode-molecule can significantly influence the charge transport characteristics in a quantum-scale system where the charge carriers can travel [1-4]. Furthermore, the interfacial characteristics affect the performance of organic electronic devices such as organic field effect transistors, organic light emitting diodes (OLED), organic photovoltaics, or organic memory [5-9]. For a better understanding and to control the charge transport properties of molecular-scale junctions, diverse approaches and testbeds have been suggested [10-12]. In particular, vertical molecular junction structures using conductive materials on top of molecules such as conducting polymers, graphene films, reduced graphene oxide, eutectic gallium and indium (EGaIn) have shown advantages in terms of high-yield molecular junctions, reliable charge transport, and junction stability [13-17]. However, despite these merits, this type of fabricated molecular junction generally uses the conductive material itself with a certain work function, which limits the potential for interface modulation because of the fixed energy band alignment between the molecular orbital level and Fermi level of the electrodes. Therefore, it is important to adopt novel conductive materials as electrode materials to achieve controllable charge transport properties. In this regard, atomically thin graphene is a promising candidate as an electrode material because it has outstanding

flexibility, transparency, conductivity, and furthermore, its electronic structure can be easily modified by chemical treatment or other external stimuli [18-20]. Therefore, a graphene electrode is suitable not only for development of reliable molecular-scale junctions but also for interface engineering, leading to the modulation of band-alignment at the graphene-molecule interface. However, it has been uncertain whether the molecular-scale junction with a doped graphene film can form a reliable molecular junction. Therefore, graphene can be a suitable material as an electrode for a reliable molecular junction by controlling the energy band alignment at the graphene-molecule interface. However, it has been uncertain whether a molecular junction with a chemically doped graphene electrode can be reliably formed or not. Once reliable molecular junctions are formed, the effect of interface engineering on the charge transport characteristics can be further investigated.

Here, we report a reliable molecular junction structure that adopt the chemical p-type doping method of a graphene film using trifluoromethanesulfonic acid (CF_3SO_3H, denoted as TFMS), which has been recently reported in some of our previous work [21]. The molecular junctions were fabricated with benzene-1,4-dithiol (denoted as BDT) self-assembled monolayers (SAMs) between the multilayer p-doped graphene (four layers) film and Au film as the top and bottom electrodes, respectively. We chose the BDT species because it is one of the simplest and well-studied conjugate molecular species of the various molecular junction platforms [22-26]. To establish different energy level alignments, we used pristine graphene (work function of ~4.4 eV) and TFMS-treated p-doped graphene (work function of ~5.23 eV) as the top electrode of the molecular junctions [21,27]. From statistical analysis, we observed noticeably enhanced charge transport properties and lowered transport barriers for the TFMS-treated p-doped graphene-electrode BDT molecular junctions. These phenomena originate from increased hole concentration and

decreased hole injection barrier at the graphene-BDT interface because the main charge transport mechanism of the junction is highest occupied molecular orbital (HOMO)-mediated non-resonant tunneling [26-28]. In addition, a comprehensive explanation was developed using the Landauer coherent transport model considering asymmetric factors and estimated transition voltage values, which was consistent with our experimental findings.

3.2. Experiments

3.2.1. Molecular Junction Fabrication

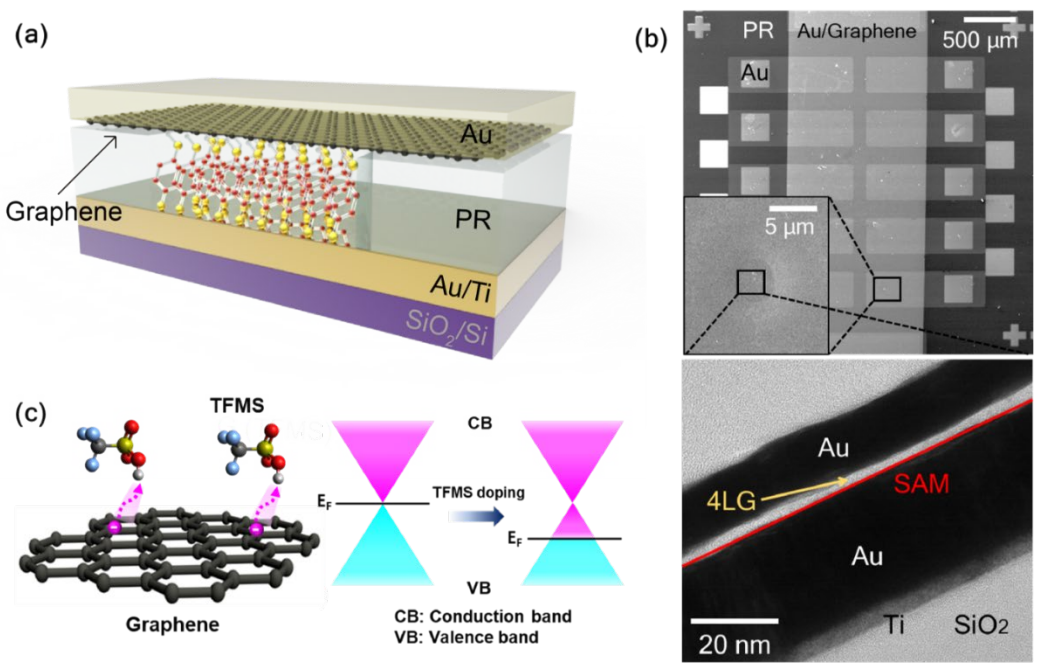

Figure 3.1. (a) Schematic of the molecular junction in this study (not scaled). (b) SEM and TEM images of fabricated molecular junctions. (c) Schematic of TFMS-doped graphene (left) and the corresponding energy band diagram shift (right).

Figure 3.1a shows a schematic of a molecular junction consisting of a vertically stacked graphene/molecules/Au structure on a SiO_2/Si substrate. The bottom electrode was made with electron-beam-evaporated Au/Ti (30 nm/5 nm) layers, then 2-μm-radius junctions were developed by photolithography and isolated by thermally hardened photoresist (AZ5214E from Az Electronic Materials) walls. On the Au surface, the BDT SAMs were deposited by a solution process with an ethanol solvent. Then, four-layered graphene films were transferred onto the samples by a four times repeated scoop-up process of single-layer graphene films which float on water. The single-layer graphene films were synthesized by a chemical vapor deposition (CVD) method. We used a four-layers-stacked graphene film as the electrode, which was based on our previous study in which we achieved high-performance OLEDs with the electrodes of four-layered graphene films rather than those with one, two, or three-layered graphene films [29]. Furthermore, there is an additional advantage of using multilayer-stacked graphene electrodes by virtue of defect-patching effect in component layers, such as point defects, polymer residues, ripples, cracks, and pores, which can be generated during graphene film synthesis and transfer [30]. When we use only single-layer graphene as the electrode, a filamentary pathway is likely to be formed when evaporating the top metal contact pad, which penetrates the junction through the inner pore of the graphene, resulting in the electrical short of most molecular junctions. However, by using multilayer graphene electrodes, this defect-patching effect enhances the coverage and homogeneity of the whole film, which then helps prevent electrical shorts and improve the reliability of the molecular junctions. Although multilayers of more than four layers may also produce similar properties, we simply used four-layer-stacked graphene as the electrode in the molecular junction, which was enough to contribute to achieving homogeneous charge injection, reproducible electrical

characteristics, and improved reliability of the junction. In this study, two types of graphene were prepared: pristine graphene films (not chemically treated) and p-doped graphene films that were chemically treated with TFMS to increase the work function and hole concentration. Chemical doping was performed after transferring graphene films onto the samples. Subsequently, the p-doped graphene films were chemically treated with TFMS. Then, the top Au (15 nm) contact pads were deposited by an e-beam evaporator and residues were removed by using reactive ion etching. Figure 3.1b shows scanning electron microscopy (SEM) and cross-sectional transmission electron microscopy (TEM) images of a completed molecular junction.

3.2.2. Characterization of the Graphene Film

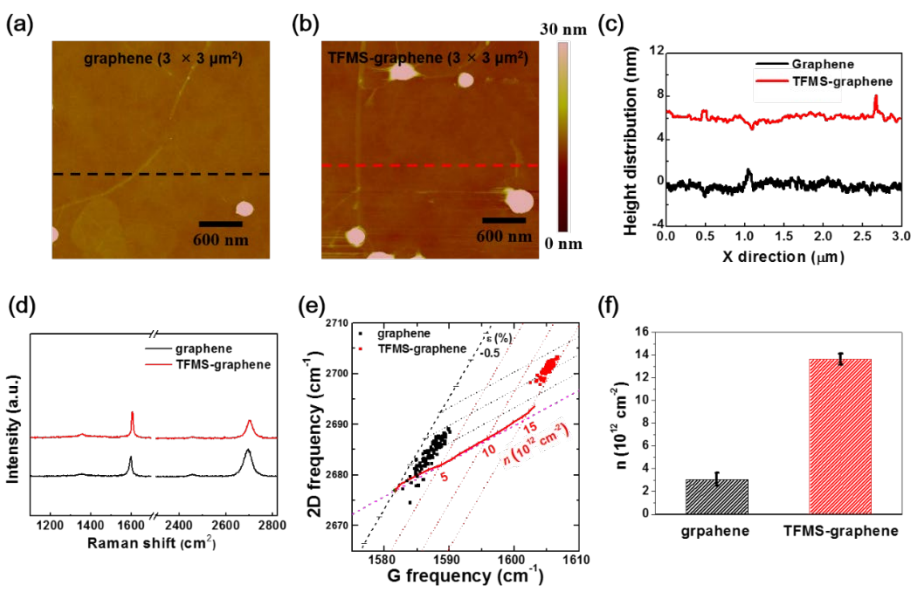

Figure 3.2. Atomic force microscopy images of (a) pristine graphene and (b) TFMS-doped graphene films. (c) Topographic profiles of these graphene films. (d) Raman spectra of a pristine graphene and TFMS-doped graphene films. (e) Pixel-to-pixel distributions of the 2D, and G mode of the pristine graphene and TFMS-doped graphene films. (f) Hole concentration of the pristine graphene and TFMS-doped graphene films.

Figure 3.1c shows a schematic of chemically p-doped graphene with TFMS and its corresponding energy band diagram before and after chemical treatment. The TFMS was dissolved in a nitromethane solvent and then spin-coated onto the graphene films. The chemical doping effect is caused by the acidic proton of the TFMS molecule, which binds to the graphene and immobilizes an equivalent quantity of electrons [21]. Since the TFMS molecules exist only on the top surface of the graphene layers, they do not affect the contact property between the SAMs and graphene electrodes. Because of the electron binding effect of the TFMS molecules, the TFMS-doped graphene results in a strong p-type doping effect with increased work function (0.83 V increase) and decreased sheet resistance (70% decrease), simultaneously retains a smooth surface without additional residues or particles and shows air stability [21]. There are two possible explanations as to how the TFMS molecules present on the top surface of the stacked graphene layers affects the Fermi level of the entire graphene layer. First, due to the intrinsic nature of graphene, the density of states of graphene is much smaller than that of metal, so the Fermi level of the entire graphene system can vary easily, even if the amount of dopant is present on the top surface [31]. Second, for the case of CVD-grown graphene, there exists various types of defects such as cracks, ripple, or inner pores. Therefore, unlike the ideal assumption that the dopants exist only on the top surface, they may actually penetrate into the inner pores inside the graphene layers and eventually affect the Fermi level of the entire system. The surface morphologies of pristine graphene and TFMS-doped graphene observed by atomic force microscopy (AFM) are shown in Figures 3.2a and 3.2b. The prepared pristine graphene and TFMS-doped graphene have clean surfaces without noticeable residues. For these images, it was confirmed that TFMS doping did not form large particles on the graphene surface. In addition, the topographic profiles along the lines in Figures 3.2a and 3.2b show that

TFMS doping did not influence the surface roughness (Figure 3.2c). Additionally, an increase in the hole concentration after TFMS treatment was verified by the raster scanning of Raman spectra. Raman spectra were obtained using a home-built setup operated with a 514-nm laser [32]. The Raman spectra of the TFMS-doped graphene film showed upshifts of the G- and 2D-bands with negligible D-bands, indicating TFMS induced p-type doping effect on graphene without generating significant defects (Figure 3.2d). To monitor the changes in hole concentration by TFMS-doping, we performed a raster-scanning of graphene and verified the distributions of the G- and 2D-band positions of each spectrum (Figure 3.2e) [32]. The changes in both the hole concentration and lattice strain can be calculated independently depending on the two different axes drawn in Figure 3.2e by using any of the measured G and 2D frequencies from Raman spectra of the graphene films [32]. By using the measured G and 2D frequencies of the graphene film change along an axis with a small slope in Figure 3.2e, the calculated hole concentration of pristine graphene and TFMS-graphene was determined as ~3×10^{12} cm^{-2} and ~1.4×10^{13} cm^{-2}, respectively. The determined hole concentration values from Figure 3.2e are summarized in Figure 3.2f, which confirms that the TFMS-doped graphene film exhibits substantially increased hole concentration.

3.3. Results & Discussions

3.3.1. Electrical Characteristics of the Graphene-electrode Molecular Junctions

As we reported previously, the dominant charge transport mechanism of the BDT molecular junctions with multilayer graphene electrodes is non-resonant tunneling, as demonstrated by molecular length- and temperature-dependent analysis, and inelastic electron tunneling spectroscopy (IETS) measurements [27]. The BDT molecular junction exhibited a decay coefficient of ~0.34 $Å^{-1}$, temperature-independent electrical characteristics, and apparent IETS peaks [27]. In the present study, we also measured the electrical properties of fabricated BDT molecular junctions and found similar charge transport characteristics. To statistically verify the effect of the p-doped graphene electrode to the charge transport of the molecular junction, we fabricated a sufficient number of molecular junctions with pristine multilayer graphene/BDT/Au (denoted as graphene/BDT/Au) and TFMS-doped multilayer graphene/BDT/Au (denoted as TFMS-graphene/BDT/Au) structures. The molecular junctions consisting of the TFMS-doped graphene electrode have been successfully fabricated with a reliable yield (> 70 %). Figures 3.3a and 3.3b show 2-dimensional current density-voltage (J-V) plots and histograms of the current values measured at 1 V of all working molecular junctions for the graphene/BDT/Au junctions; Figures 3.3c and 3.3d show the data for the TFMS-graphene/BDT/Au junctions. The inset graphs in Figures 3.3a and 3.3c depict the averaged J-V curves for these two types of molecular junctions. The average current density for the graphene/BDT/Au junctions was found to be 1.7×10^4 A/m^2 at 1 V, whereas for the TFMS-graphene/BDT/Au junctions, the average current density was found to be 2.0×10^5 A/m^2 at 1 V, which shows clearly enhanced charge transport characteristics when using the p-doped

graphene electrode. The average current density was increased order of magnitude for the TFMS-doped graphene-electrode molecular junctions compared to that of the pristine graphene-electrode molecular junctions. In addition, the averaged low-voltage (from -0.3 V to 0.3 V) resistance of the TFMS-graphene/BDT/Au junctions was an order of magnitude lower than that of graphene/BDT/Au junctions.

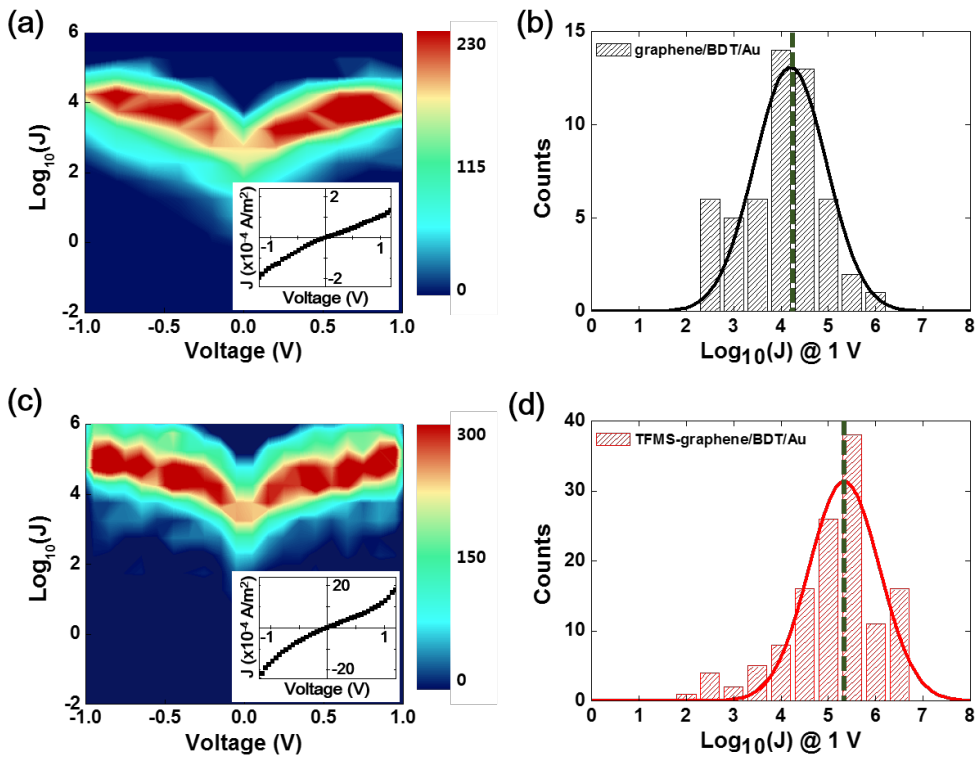

Figure 3.3. (a,c) Two-dimensional J-V plots of the working molecular junctions for the (a) graphene/BDT/Au and (c) TFMS-graphene/BDT/Au junctions. The inset is the average J-V curve from the measured data. (b,d) Histogram of the current density at 1 V of the working molecular junctions of the (b) graphene/BDT/Au and (d) TFMS-graphene/BDT/Au junctions.

3.3.2. Transition Voltage Spectroscopy Analysis of the Graphene-electrode Molecular Junctions

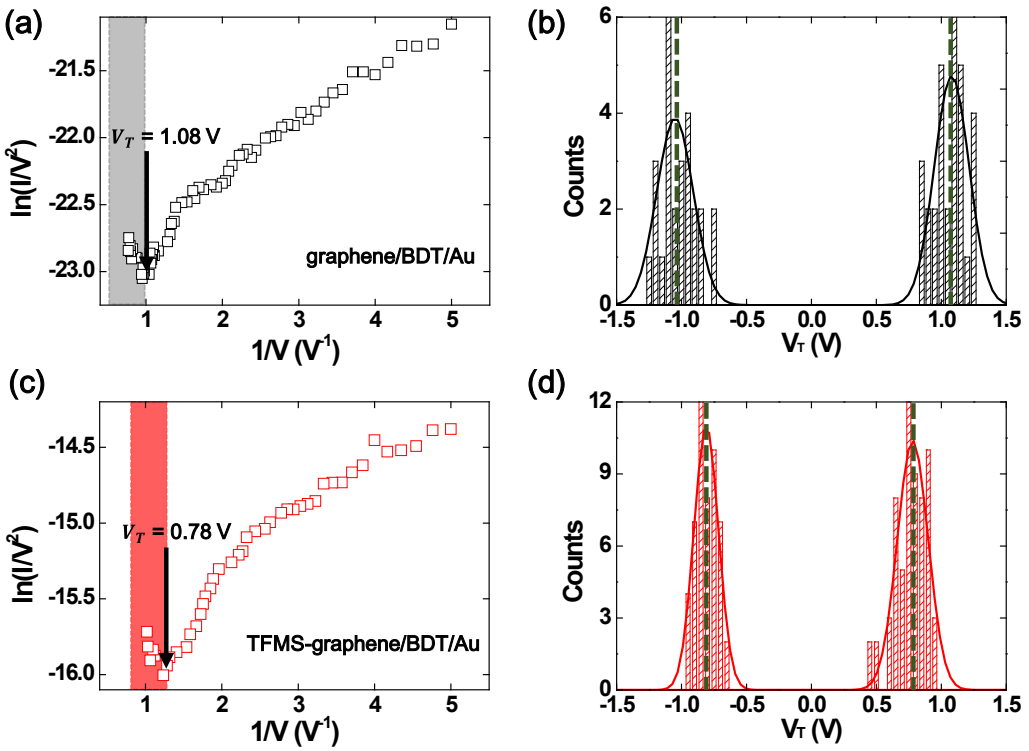

Figure 3.4. (a,c) The representative TVS data of the (a) graphene/BDT/Au and (c) TFMS-graphene/BDT/Au junctions. (b,d) Histograms of V_T for the (b) graphene/BDT/Au and (d) TFMS-graphene/BDT/Au junctions for both voltage bias.

For better insight into the enhanced charge transport phenomena, we performed transition voltage spectroscopy (TVS) analysis to estimate the BDT SAMs were deposited by a solution process with an ethanol solvent. effective barrier height (i.e., the offset between the Fermi energy of the electrode (E_F) and energy level of the HOMO (E_{HOMO})) at the electrode-molecule interface. By converting the J-V curve into Fowler-Nordheim (F-N) plot, the transition voltage (V_T) can be obtained from the inflection point of the F-N plot, which equals the barrier height when applying the Simmons tunneling model [33-34].

Alternatively, by adopting the coherent transport model for the molecular junctions, [35-37] in which the charge transport is determined by a transmission function that depends on the molecular energy orbital levels and degree of electrode-molecule interface coupling, the V_T (i.e., the inflection point in the F-N plot) is found to be the point where a certain tail of the integral of the transmission function enters into the bias window. The V_T value is therefore closely associated with the barrier height and the amount of coupling at the electrode-molecule interface. In this regard, TVS can be used to investigate the energy level alignment of the molecular junctions and the interfacial asymmetry characteristics of the couplings. Figures 3.4a and 4b show a representative F-N plot and a statistical histogram for V_T values determined from TVS for the graphene/BDT/Au molecular junctions.

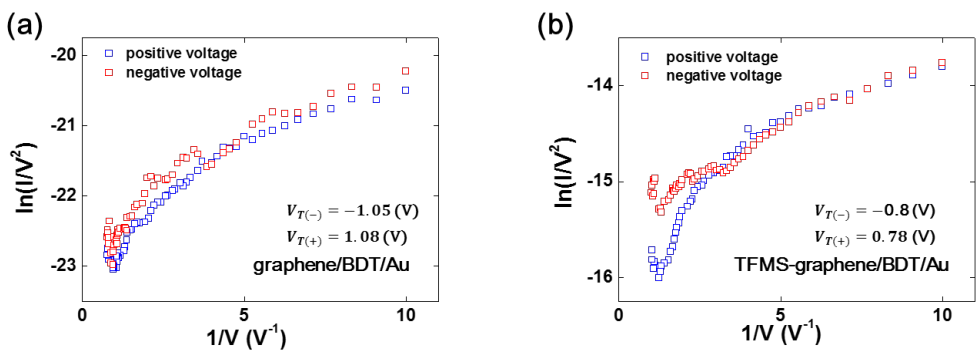

Figure 3.5. The representative TVS data of both positive and negative voltage regions for (a) graphene/BDT/Au junction and (b) TFMS-graphene/BDT/Au junctions.

The average value of V_T was found to be ~1.08 V and was symmetric for positive and negative voltage polarities (see Figure 3.5a). Figures 3.4c and 3.4d show similar data for the TFMS-graphene/BDT/Au molecular junctions. The averaged value of V_T was found to be ~0.78 V for both voltage polarities (also see Figure 3.5b), which was ~0.3 V lower than that of the graphene/BDT/Au junctions. These results are logical because the work

function of the p-doped graphene electrode was increased; therefore, the charge injection barrier was lowered in the HOMO-dominating molecular junctions. Our findings are also consistent with the experimental data given by Beebe et al [27-28] and Kim et al [37], which show a linear relationship between V_T and the metal electrode's work function.

3.3.3 Theoretical Interpretation Based on the Coherent Transport Model

The charge transport properties in the molecular system can be interpreted from the Landauer formula, which describes an I-V relationship with an integral of the transmission function of the molecular orbital within the bias windows [35-36, 39].

$$\mathrm{I} = \frac{2e}{h}\int_{-\infty}^{\infty} T(E)[f_1(E) - f_2(E)]dE \quad . \tag{1}$$

Here, $f_{1,2}(E) = (1 + \exp(E - \mu_{1.2})/kT)^{-1}$ is the Fermi-Dirac distribution function where $\mu_{1,2}$ is the chemical potential for each contact electrode. In addition, T(E) is the transmission function that has Lorentzian-shaped peaks around the molecular orbitals as

$$\mathrm{T(E)} = \sum_n \frac{\Gamma_{n,1}\Gamma_{n,2}}{[{\Gamma_n}^2/4 + (\mathrm{E} - \mathrm{E_n})^2]} \ , \tag{2}$$

where n indicates each molecular energy level and $\Gamma_{n,1 \text{ or } 2}$ denotes the energy broadening corresponding to the molecule-electrode coupling at both sides ($\Gamma_n = \Gamma_{n,1} + \Gamma_{n,2}$ means the total broadening). In a symmetric molecular junction, $\Gamma_{n,1}$ and $\Gamma_{n,2}$ are equal. If the junction is more strongly coupled with one electrode than the other, the transmission function will be asymmetrically broadened. Therefore, it is reasonable to denote $\Gamma_{n,1} = \eta\ \Gamma_n$ and $\Gamma_{n,2} = (1 - \eta)\ \Gamma_n$, where $\eta\ (0 \le \eta \le 0.5)$ is an asymmetry factor (if the junction is symmetric, $\eta = 0.5$). Furthermore, the position of the molecular orbital will be shifted following the chemical potential of a strongly coupled electrode by

the amount of $(1/2-\eta)$ V. Assuming only the frontier molecular orbitals (i.e., HOMO and lowest unoccupied molecular orbital (LUMO)) are involved in charge transport and the transmission decays exponentially with molecular length, the T(E) can be expressed as follows [35].

$$
\begin{aligned}
&T(E,V) \\
&= \frac{1}{\frac{1}{4\eta(1-\eta)} + \left(\frac{E-(E_{HOMO}+(1/2-\eta)\times V)}{E_F-(E_{HOMO}+(1/2-\eta)\times V)}\right)^2 \exp(2\sqrt{2m(E_F-E_{HOMO})}d/\hbar)} \\
&+ \frac{1}{\frac{1}{4\eta(1-\eta)} + \left(\frac{E-(E_{LUMO}+(1/2-\eta)\times V)}{E_F-(E_{LUMO}+(1/2-\eta)\times V)}\right)^2 \exp(2\sqrt{2m(E_{LUMO}-E_F)}d/\hbar)}
\end{aligned}
\quad (3)
$$

where E_F is the average Fermi energy of both electrodes and d is the molecular length. Using this formula, we calculated T(E) and I-V curves of the graphene/BDT/Au and TFMS-graphene/BDT/Au junctions, then V_T values were determined at the F-N plots from the calculated I-V curves. The results of these calculations are provided in the Figures 3.6~3.8.

In the calculation, the Fermi energy E_F was the average of Au and graphene, or Au and TFMS-graphene. The E_F of Au, graphene, and TFMS-graphene was 5.1 eV, 4.4 eV, and 5.23 eV, respectively. And the highest occupied molecular orbital (HOMO) level and the lowest unoccupied molecular orbital (LUMO) level of the BDT molecule were set to 6.0 eV and 3.6 eV below from the vacuum level (defined as zero eV), respectively. The molecular length d was 0.5 nm. By inserting these values, T(E) was calculated for η = 0.1, 0.2, 0.3, 0.4, and 0.5 (Figure 3.6).

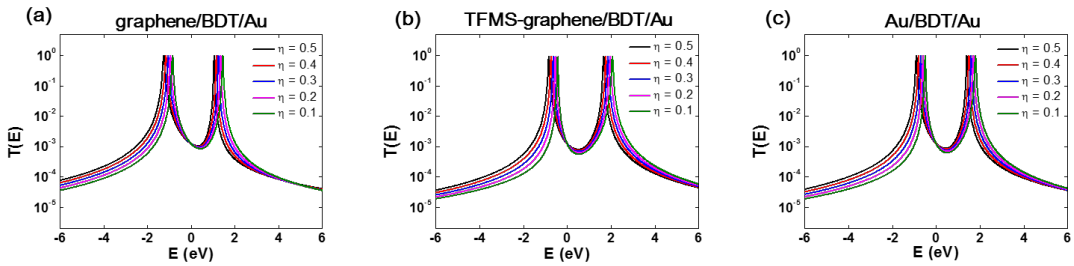

Figure 3.6. Calculated T(E) for (a) graphene/BDT/Au, (b) TFMS-graphene/BDT/Au, and (c) Au/BDT/Au molecular junctions.

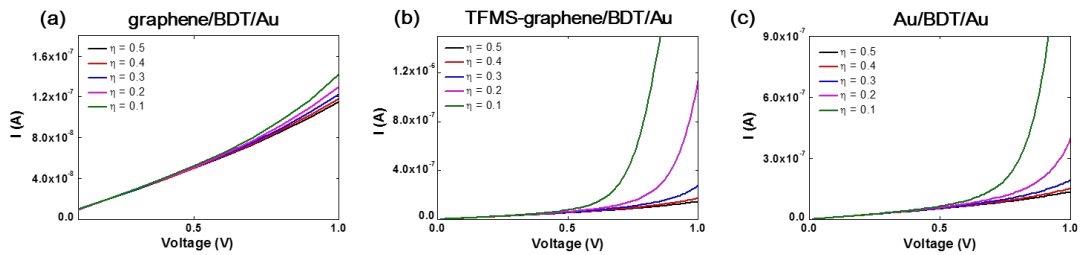

Figure 3.7. Calculated I(V) for (a) graphene/BDT/Au, (b) TFMS-graphene/BDT/Au, and (c) Au/BDT/Au molecular junctions.

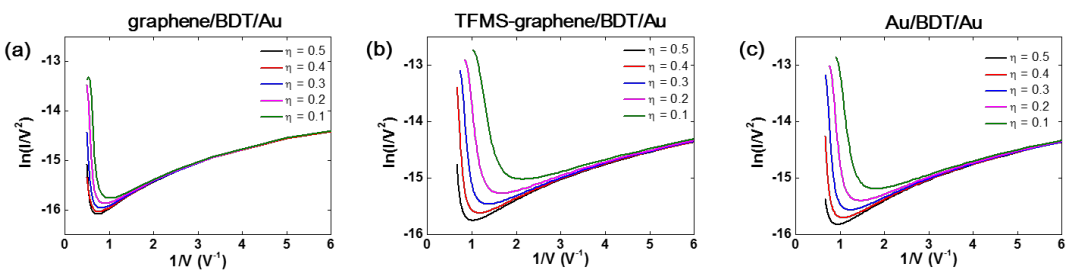

Figure 3.8. Calculated FN plots for (a) graphene/BDT/Au, (b) TFMS-graphene/BDT/Au, and (c) Au/BDT/Au molecular junctions.

By integrating these T(E) curves into the Landauer formula, the calculated I-V curves are given as Figure 3.7. By switching I-V curve to FN plot (Figure 3.8), the transition voltage which is the inflection point of the plot were determined for graphene/BDT/Au, TFMS-graphene/BDT/Au, and Au/BDT/Au molecular junctions for η

= 0.1, 0.2, 0.3, 0.4, and 0.5.

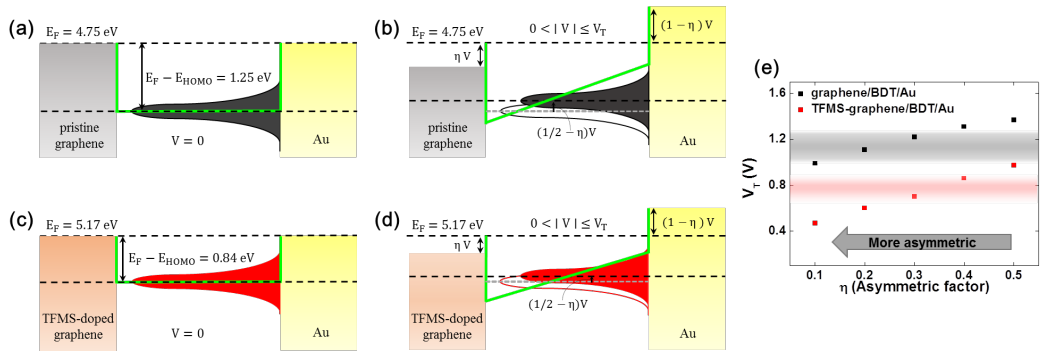

Figure 3.9. (a,c) The energy band diagram of the (a) graphene/BDT/Au and (c) TFMS-graphene/BDT/Au junctions at zero voltage. (b,d) The energy band diagrams of the (b) graphene/BDT/Au and (d) TFMS-graphene/BDT/Au junctions when a finite voltage below the V_T is applied. (e) The V_T versus η graphs of the graphene/BDT/Au (black symbols) and TFMS-graphene/BDT/Au junctions (red symbols) calculated based on the Landauer formula. Colored areas on the graph indicate the experimental results.

In Figures 3.9a–3.9d, the Landauer transport model is depicted with appropriate energy band diagrams. Figures 3.9a and 3.9c show the energy band diagram of the graphene/BDT/Au, and TFMS-graphene/BDT/Au junction at zero voltage, respectively. The hole injection barrier height was set at 1.25 eV (graphene/BDT/Au), and 0.84 eV (TFMS-graphene/BDT/Au), which is the offset between the HOMO of BDT (6.0 eV) and the average Fermi energy of the electrodes (E_F values of Au, pristine graphene, and TFMS-graphene were 5.10 eV, 4.40 eV, and 5.23 eV, respectively). Note that for mixed electrodes, it is reasonable to assume that an average work function equals the work function of the electrodes in the entire molecular junction system [38, 40]. The transmission function (shown as a black/red curve in Figure 3.9a/c) of BDT is Lorentzian–shaped and strongly coupled to the Au electrode; the peak position matches the HOMO level. The green solid

line represents the effective tunneling barrier in the rectangular barrier shape at zero voltage. Figures 3.9b and 3.9d show the energy band diagram of the graphene/BDT/Au, and TFMS-graphene/BDT/Au junctions, respectively, when a finite voltage below V_T is applied. In this case, the shape of the effective tunneling barrier changes from rectangular to trapezoidal. Here, the rise and drop of the energy bands for both electrodes are asymmetric with an amount corresponding to the asymmetric factor η. At the same time, the molecular level will follow the chemical potential of the strongly coupled Au electrode by an amount of $(1/2 - \eta)$ V (see the shift of the transmission function from the unfilled to the filled red curve in Figures 3.9b and 3.9d). As the asymmetry increases, the coupling between the graphene electrode and molecular orbital becomes weaker, then the intensity of the transmission function peak will decrease. On the other hand, if a junction is symmetric, the molecular level will remain at the zero-voltage position. When the voltage reaches V_T, the barrier changes from a trapezoidal barrier to a triangular barrier and a transition to F-N tunneling will occur. In Figure 3.9e, the calculated values of V_T are plotted versus η for the graphene/BDT/Au and TFMS-graphene/BDT/Au junctions derived from the calculated T(E) and I-V data (Figures 3.6 and 3.7). The colored areas on the graph indicate the distribution of experimental V_T values of the graphene/BDT/Au and TFMS-graphene/BDT/Au junctions within the standard deviations. With this graph, we found a good consistency between the coherent Landauer model and the experimental results. Particularly, the calculation results agreed well with experimental data, when $\eta \cong 0.2$ for graphene/BDT/Au and $\eta \cong 0.3$ for the TFMS-graphene/BDT/Au junction. Note that the difference in η values (0.2 versus 0.3) suggests that the couplings between the graphene/BDT/Au and TFMS-graphene/BDT/Au junctions are different. Although the selected η values successfully matched the transition voltages measured from the TVS

analysis, there is a possibility that the selected η value itself may be different with 'actual' η value because the coherent model does not consider any barrier lowering effects resulting from the image potential, etc. Furthermore, the contact geometry of molecules on the electrode can also affect the shape of the transmission function. Therefore, the coherent model may predict a relatively lower transition voltage for a given η value [35] Although the η value may be different from the actual η value as mentioned, it can be reasonably verified that the coherent model can explain the reduction (by ~0.3 V) in the effective barrier height of molecular junction with the TFMS-doped graphene electrode.

3.4. Conclusion

In summary, we fabricated and characterized vertical-type molecular junctions composed of BDT SAMs with multilayer graphene film electrodes. The chemically p-doped TFMS-graphene was used as the electrode material. The electrical characteristics of the molecular junctions with pristine graphene and TFMS-graphene electrodes were statistically analyzed. From that, the enhanced charge transport properties were observed in the case of the TFMS-graphene electrode molecular junctions, as a result of a lowered charge injection barrier in the HOMO-dominating molecular junctions. A theoretical analysis based on the coherent transport model that considered asymmetric couplings at the electrode-molecule interfaces demonstrated the validity of these results. Our study provides promising insight for the control of charge transport by interface engineering in reliable molecular junction platforms.

References

(1) Lindsay, S. M.; Ratner, M. A., **2007,** *19*, 23-31.

(2) Hihath, J.; Tao, N., *Semicond. Sci. Technol.* **2014,** *29*, 054007.

(3) Aradhya, S. V.; Frei, M.; Hybertsen, M. S.; Venkataraman, L., *Nat. Mater.* **2012,** *11*, 872-876.

(4) Jia, C.; Guo, X., *Chem. Soc. Rev.* **2013,** *42*, 5642-5660.

(5) Ma, H.; Yip, H. L.; Huang, F.; Jen, A. K. Y., *Adv. Funct. Mater.* **2010,** *20*, 1371-1388.

(6) Facchetti, A., *Chem. Mater.* **2011,** *23*, 733-758.

(7) Ho, P. K.; Kim, J.; Burroughes, J. H.; Becker, H., *Nature* **2000,** *404*, 481-484.

(8) Cho, B.; Song, S.; Ji, Y.; Kim, T. W.; Lee, T., *Adv. Funct. Mater.* **2011,** *21*, 2806-2829.

(9) Di, C.-a.; Liu, Y.; Yu, G.; Zhu, D., *Acc. Chem. Res.* **2009,** *42*, 1573-1583.

(10) Cui, X. D.; Primak, A.; Zarate, X.; Tomfohr, J.; Sankey, O. F.; Moore, A. L.; Moore, T. A.; Gust, D.; Harris, G.; Lindsay, S. M., *Science* **2001**, *294*, 571-574

(11) Chen, J.; Reed, M. A.; Rawlett, A. M.; Tour, J. M., *Science* **1999,** *286* (5444), 1550-1552.

(12) Haag, R.; Rampi, M. A.; Holmlin, R. E.; Whitesides, G. M., *J. Am. Chem. Soc.* **1999**, *121*, 7895-7906.

(13) Yoon, H. J.; Shapiro, N. D.; Park, K. M.; Thuo, M. M.; Soh, S.; Whitesides, G. M., *Angew. Chem. Int. Ed.* **2012,** *51*, 4658-4661.

(14) Akkerman, H. B.; Blom, P. W. M.; de Leeuw, D. M.; de Boer, B. *Nature* **2006,** *441*, 69-72.

(15) Wang, G.; Kim, Y.; Choe, M.; Kim, T. W.; Lee, T. A., *Adv. Mater.* **2011,** *23*, 755-760.

(16) Seo, S.; Min, M.; Lee, J.; Lee, T.; Choi, S. Y.; Lee, H., *Angew. Chem. Int. Ed.* **2012,** *51*, 108-112.

(17) Thuo, M. M.; Reus, W. F.; Nijhuis, C. A.; Barber, J. R.; Kim, C.; Schulz, M. D.; Whitesides, G. M., *J. Am. Chem. Soc.* **2011,** *133*, 2962-2975.

(18) Bae, S.; Kim, H.; Lee, Y.; Xu, X.; Park, J. S.; Zheng, Y.; Balakrishnan, J.; Lei, T.; Kim, H. R.; Song, Y. I.; Kim, Y.-J.; Kim, K. S.; Özyilmaz, B.; Ahn, J.-H.; Hong, B. H.; Iijima, S., *Nat. Nanotechnol.* **2010,** *5*, 574-578.

(19) Han, M. Y.; Özyilmaz, B.; Zhang, Y.; Kim, P., *Phys. Rev. Lett.* **2007,** *98*, 206805.

(20) Lin, Y.-C.; Lin, C.-Y.; Chiu, P.-W., *Appl. Phys. Lett.* **2010,** *96*, 133110.

(21) Han, T. H.; Kwon, S. J.; Li, N.; Seo, H. K.; Xu, W.; Kim, K. S.; Lee, T. W., *Angew. Chem. Int. Ed.* **2016,** *55*, 6197-6201.

(22) Martin, C. A.; Ding, D.; van der Zant, H. S. J; van Ruitenbeek, J. M., *New J. Phys.* **2008,** *10*, 065008.

(23) Bratkovsky, A. M.; Kornilovitch, P. E., *Phys. Rev. B* **2003,** *67*, 115307.

(24) Kim, Y.; Pietsch, T.; Erbe, A.; Belzig, W.; Scheer, E., *Nano Lett.* **2011,** *11*, 3734-3738.

(25) Xiao, X.; Xu, B.; Tao, N. J., *Nano Lett.* **2004,** *4*, 267-271.

(26) Reddy, P.; Jang, S.-Y.; Segalman, R. A.; Majumdar, A., *Science* **2007,** *315*, 1568-1571.

(27) Jang, Y.; Jeong, H.; Kim, D.; Hwang, W.-T.; Kim, J.-W.; Jeong, I.; Song, H.; Yoon, J.; Yi, G.-C.; Jeong, H.; Lee, T., *Nanotechnology* **2016,** *27*, 145301.

(28) Malen, J. A.; Doak, P.; Baheti, K.; Tilley, T. D.; Majumdar, A.; Segalman, R. A., *Nano Lett.* **2009,** *9*, 3406-3412.

(29) Han, T. H.; Lee, Y.; Choi, M. R.; Woo, S. H.; Bae, S. H.; Hong, B. H.; Ahn, J. H.; Lee, T. W., *Nat. Photon.* **2012,** *6*, 105-110.

(30) Seo, H. K.; Park, M. H.; Kim, Y. H.; Kwon, S. J.; Jeong, S. H.; Lee, T. W., *ACS Appl. Mater. Interfaces* **2016,** *8*, 14725-14731.

(31) Neto, A. H. C.; Guinea, F.; Peres, N. M. R.; Novoselov, K. S.; Geim, A. K., *Rev. Mod. Phys.* **2009**, *81*, 109-162.

(32) Lee, J. E.; Ahn, G.; Shim, J.; Lee, Y. S.; Ryu, S., *Nat. Commun.* **2012**, 3, 1024.

(33) Beebe, J. M.; Kim, B.; Frisbie, C. D.; Kushmerick, J. G., *ACS Nano* **2008,** *2*, 827-832.

(34) Beebe, J. M.; Kim, B.; Gadzuk, J. W.; Frisbie, C. D.; Kushmerick, J. G., *Phys. Rev. Lett.* **2006,** *97*, 026801.

(35) Wang, G.; Kim, Y.; Na, S.-I.; Kahng, Y. H.; Ku, J.; Park, S.; Jang, Y. H.; Kim, D.-Y.; Lee, T., *J. Phys. Chem. C* **2011,** *115*, 17979-17985.

(36) Huisman, E. H.; Guédon, C. M.; van Wees, B. J.; van der Molen, S. J., *Nano Lett.* **2009,** *9*, 3909-3913.

(37) Bâldea, I., *Phys. Rev. B* **2012,** *85*, 035442.

(38) Kim, B.; Choi, S. H.; Zhu, X.-Y.; Frisbie, C. D., *J. Am. Chem. Soc.* **2011,** *133*, 19864-19877.

(39) Chen, J.; Markussen, T.; Thygesen, K. S., *Phys. Rev. B* **2010,** *82*, 121412.

(40) Engelkes, V. B.; Beebe, J. M.; Frisbie, C. D., *J. Am. Chem. Soc.* **2004,** *126*, 14287-14296

Chapter 4. Unidirectional Real-Time Photoswitching of Diarylethene Molecular Monolayer Junctions with Multilayer Graphene Electrodes

4.1. Introduction

To achieve the ultimate miniaturization of electronic devices, a wide range of studies in the field of molecular electronics has been carried out over the last decades. Important developments include utilization of functional molecules for realizing molecular wires, rectifiers, switches, transistors, and thermoelectric devices [1-10]. Among such developments, the molecular switch is a promising building block due to its potential as a memory device. Usually, a molecular switch consists of two stable isomers and undergoes a transition between them upon exposure to an external stimulus such as light, heat, or an electric field [11-13]. In particular, light is useful for switching devices because of its addressability and compatibility with solid-state device structures. Therefore, the design of photochromic molecules is important for molecular switching devices. DAEs form a class of photochromes with two different conductance states, i.e., a high conductance (closed; ON) and a low conductance (open; OFF) state. In solution, DAEs can be converted between these two states by illumination with UV or visible light, respectively. This property makes them good candidates for photoswitching devices due to a large conductance difference between the two states and their response to light [14-16].

As promising photoswitching molecules, DAEs have been utilized in various ways with the aim to demonstrate bidirectional switching in molecular devices. For an Au-DAE-

Au junction, only a unidirectional switching from the closed to the open state has been observed [17]. Subsequent theoretical studies have explained this nonreversability of the DAE molecular junction by the strong coupling between the molecule and the metallic electrode which leads to quenched molecular states [18-19]. On the other hand, unidirectional switching from the low- to the high-conductance state in Au-DAE-Au single-molecule junctions was obtained by modifying the side-arms and end-groups such that they form rigid conjugated molecular wires [20]. These molecules feature a very high quantum yield for the ON switching reaction, but a relatively low one for the OFF switching, explaining the inversed unidirectional switching. In addition, a similar single DAE molecule, bridged between carbon nanotubes [15] or graphene sheets [21], showed a unidirectional switching from the open to the closed state, because strong molecule-electrode couplings between closed state DAE and graphene electrodes enabled the energy transfer from the photoexcited molecule to the extended π-electron system in the electrodes [7, 21]. To overcome this unidirectional switching in DAE molecular junctions, various attempts were made. For example, through the introduction of a cross-conjugated system into the DAE molecule, namely meta-substituted phenyl end groups, the high conductance state could be stabilized and thereby reversible switching in arrays of Au-DAE-Au junctions was demonstrated [22]. For DAE junctions with graphene electrodes, the unidirectional switching properties could be turned into bidirectional switching by adding alkane groups into both sides of the molecular backbone [7]. This series of studies demonstrates that the side-arms and end-groups, which provide the coupling between the molecule and the electrodes, play an important role in the switching characteristics since they control the energetic alignment between the Fermi level and the current-carrying molecular orbitals as well as the molecular orbitals' linewidth broadening [20, 23].

Molecular photoswitching devices have been developed beyond single-molecule junctions to realize large-area molecular junctions based on DAE molecules. Kronemeijer et al. demonstrated reliable bidirectional photoswitching for such large-area molecular junctions processed with SAMs of DAEs, when poly(3,4-ethylenedioxythiophene):poly(styrene sulfonate) (PEDOT:PSS) was used as a top interlayer in addition to Au electrodes [24]. However, in our recent work on slightly modified DAE molecules, we found no optically-induced switching although the junction structure was the same as above [16]. This observation indicates that the mechanisms behind the photoswitching phenomenon in large-area molecular junctions still remain elusive.

We have previously reported the observation of bidirectional photoswitching behavior in DAE molecular junctions fabricated via self-assembly on an Au bottom electrode with a reduced graphene oxide (rGO) top electrode, which can withstand external mechanical stress [25]. In the present study, we employ multilayer graphene (MLG) as the top electrode in the molecular junction, which shows a superior optical transmittance and higher conductance than that of the rGO electrode. At the same time, however, we find that the junction no longer exhibits the bidirectional switching behavior; instead, the device can only be switched from the OFF to the ON state, i.e., from the open to the closed state of the employed 1,2-bis(2-methyl-5-(4-mercaptophenylethynyl)furan-3-yl)perfluorcyclopent-1-ene DAE. By performing a quantitative analysis in terms of a Landauer coherent transport model, we attribute the unidirectionality mainly to an increased electronic coupling between the closed state of the molecule and the MLG electrode as compared to the situation for rGO.

4.2. Experiments

4.2.1. Synthesis of MLG

The MLG film was synthesized by chemical vapor deposition (CVD) on catalytic metal surfaces [26-31]. Ni (300 nm)/Ti (20 nm) substrates purchased from Jinsol, Inc. were cleaned respectively in acetone, methanol, 2-propanol, and deionized water with an ultrasonicator for 10 min each. Then, the substrates were loaded into a CVD system (Teraleader Co., Korea) and preheated at 500 °C with a 200 sccm stream of Ar/H_2 at 800 Torr for ~30 min to eliminate the oxidized layer on the Ni surface. Afterwards, the MLG films were grown under a gas flow of 15 sccm CH_4 and 20 sccm Ar/H_2 at 20 Torr for 5 min at 900 °C.

4.2.2. Molecular Junction Fabrication

Figure 4.1a shows a brief schematic diagram of the fabrication procedure used for the molecular junctions described in this study. We followed the well-established fabrication process that we have previously reported [32-33] We chose poly(ethylene-2,6-naphthalate) (PEN) (Q83 purchased from Teijin DuPont Film Co., Ltd.) as a substrate material for the molecular junctions to enable operation even under mechanically flexible conditions. Au (50 nm)/Ti (5 nm) bottom electrodes were deposited onto the PEN substrates at a slow deposition rate of ~0.2 Å/s using an electron beam evaporator. Next, a photoresist (PR) was spin-coated onto the surface, and circular holes with a radius of 10 μm were created on the PR film to expose the surface of the Au electrode by photolithography. The patterned samples were hard-baked at 190 °C for ~2 h to enhance the chemical resistance to the SAM solution. For the SAM deposition, each sample was dipped into a diluted DAE solution (~3 mM in ethanol solvent) for 24 h in a N_2-filled glove box with a few drops of

ammonium hydroxide (NH_4OH) added into the solution, which is required to deprotect the acetyl group from the thiol end group. The molecular structure of the DAE under study is illustrated in Figure 4.1c.

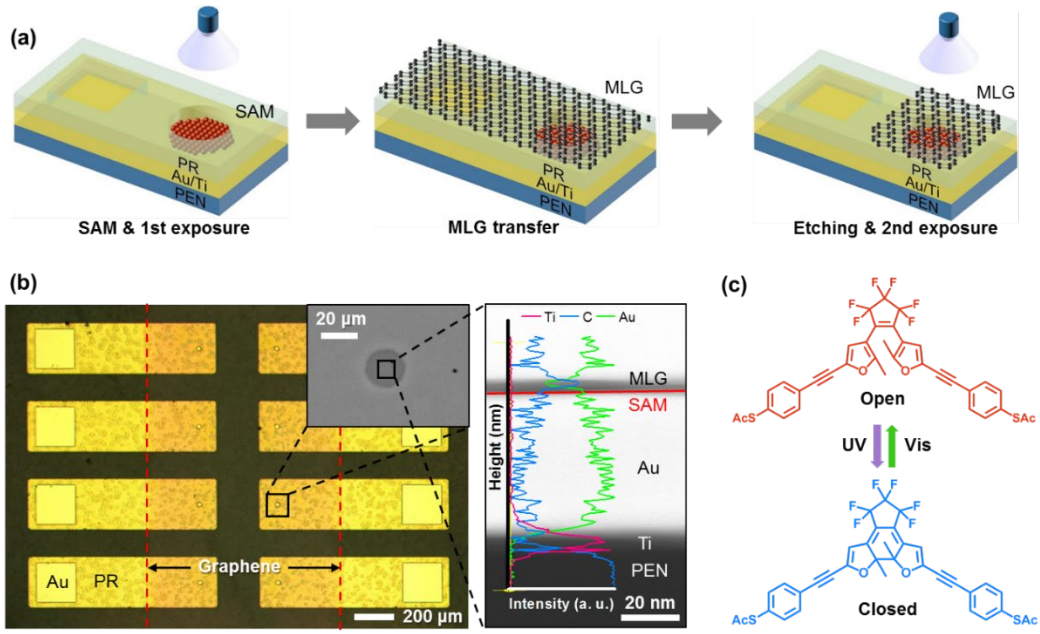

Figure 4.1. (a) Schematic representation of the fabrication process for the molecular junctions. (b) Optical (left), SEM (inset), and a cross-sectional TEM (right) image of the fabricated molecular junctions. The TEM image is superimposed with an atomic composition profile measured by EDS. (c) The chemical structures of the DAE molecule in the open (top) and closed (bottom) state.

As described in detail in a previous paper [34] the DAE molecules are known to be attached via S-Au bonds to Au surfaces and form a somewhat disordered monolayer. Furthermore, X-ray photoelectron spectroscopy (XPS) and model calculations for DAE were presented in Kronemeijer et al [24] In that paper, the experimentally estimated molecular layer thickness from the analysis of XPS data was ~2.0 nm for the closed state and ~2.4 nm the open state. This result implies that the DAE in the closed state exhibits a

more tilted off-normal angle than the open state. Also, this observation implies that the molecules are in a “standing” configuration with only one thiol bound to the Au electrode, instead of a “lying-down” one with both thiols bound to the metal. Afterwards, we softly rinsed the samples with anhydrous ethanol and exposed each sample to 360 nm UV or 520 nm visible light to induce the closed or open state, respectively. Next, the MLG film was transferred to the molecular layer to make a contact through van der Waals interaction. The detailed procedure for preparing the transfer will be described in the following section. The unnecessary MLG part was removed via a shadow mask by means of an oxygen plasma treatment (under 10 sccm of O_2 gas at 50 W of power) to define each junction. Lastly, we once more exposed each sample to light (UV or visible) to ensure that the molecules remained in the desired state. The entire process after the SAM deposition was conducted in the dark to avoid undesirable effects caused by light exposure. Figure 4.1b shows the images of the fabricated molecular junctions obtained from optical microscopy, scanning electron microscopy (SEM), and cross-sectional transmission electron microscopy (TEM). From the atomic composition profile determined from energy-dispersive X-ray spectroscopy (EDS) along the cross section shown in Figure 4.1b, we could confirm that the C-rich part exists in the MLG and SAM layer between the surrounding Au parts. On the other hand, it was observed that the relative proportion of Au atoms decreased in these layers. This observation indicates that the MLG and SAM layers were well deposited and clearly distinguishable from the Au electrode. The Au peak at the top reflects an Au protection layer, needed for the EDS measurement and deposited using a focused ion beam process.

4.2.3. Preparation of the MLG Top Electrode

The MLG film of the previous section is synthesized on Ni substrates. Subsequently, it is spin-coated with poly(methyl methacrylate) (PMMA, 950PMMA A5 from MicroChem Corp.) as a dummy layer. The Ni layer beneath the MLG film was etched by an iron (III) chloride ($FeCl_3$) aqueous solution. The floating MLG film, detached from the substrate, was rinsed with deionized (DI) water more than three times to eliminate the adhered Fe and Ni ions. Then, the cleaned MLG film was placed onto the molecular layer as the top electrode of the molecular junction. After drying for a few hours to ensure good contact with the molecules, the PMMA layer was removed with acetone and isopropyl alcohol (IPA).

4.2.4. Electrical Characterization

The electrical characteristics of the molecular junctions were measured with a semiconductor parameter analyzer (Keithley 4200 SCS) and a probe station system (JANIS Model ST-500) under ambient conditions.

4.3. Results & Discussions

4.3.1. Characterization of MLG Electrode

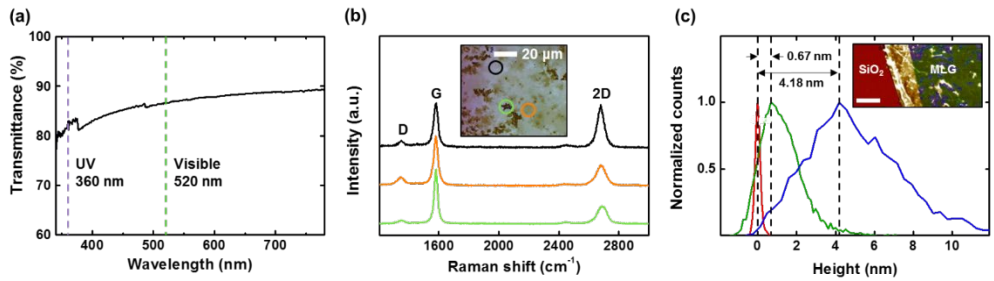

Figure 4.2. (a) The measured optical transmittance of a MLG film on a glass substrate. (b) Raman spectra for three different areas of a MLG film. (c) A topographic profile of a MLG film. The white scale bar in the inset image represents 4 μm.

As depicted in Figure 4.2, we have investigated the optical and morphological traits of the MLG film to confirm its suitability for use as the top electrode in Au-DAE-MLG junctions. Figure 4.2a presents the optical transmittance of the MLG film measured under light illumination over a wavelength range from 340 to 780 nm. Since the MLG film shows a transmittance of more than 80% at both 360 nm and 520 nm, the material can be considered adequately transparent at the wavelengths at which the state of DAE can be transformed. The typical D, G, and 2D peaks of the MLG film in the Raman spectrum at energy shifts of 1350, 1580, and 2680 cm^{-1}, respectively, are shown in Figure 4.2b. The individual colored lines in this graph indicate the Raman peaks for the corresponding areas in the optical microscope (OM) image shown in the inset. The region marked by a black circle in the OM image has similar intensities for the G and 2D peaks in the Raman spectrum (black line). This indicates that the MLG film in that region is relatively thin and can be regarded as triple-layer graphene. On the other hand, the height of the 2D peaks is approximately half of those of the G peaks in the green and orange encircled regions in the

OM image, and thus these areas are considered to be thicker multilayers [35]. Figure 4.2c shows the topographic profile of a MLG film transferred onto a SiO_2/Si substrate. Each colored line in the graph represents the area marked with the same color in the atomic force microscope (AFM) image shown in the inset. The normalized count denotes the number of pixels for a certain height in each area divided by the maximum value of counts as obtained over all heights. This analysis shows that most of the area marked in green in the inset image has a thickness of 0.67 nm, which is similar to that of a monolayer of graphene, and that the small areas marked in blue have a thickness of 4.18 nm. When zooming in on the area of the green region, we find many multilayer features. Therefore, the results are in agreement with earlier reports that the MLG film, grown on a Ni substrate, is non-uniform, rather thick and optically transparent [26].

4.3.2. Photoswitching Properties of DAE Molecular Junctions

The current density-voltage (*J-V*) characteristics and their histograms for the DAE molecular junctions with an MLG top electrode are shown in Figure 4.3. The *J-V* data were obtained from the open and closed state junctions, fabricated separately. Figure 4.3a shows the histograms of the current density values for each state measured at 1 V from the entire set of working molecular junctions (131 molecular junctions in the open state and 111 molecular junctions in the closed state). Nonworking molecular junctions can be easily recognized as short-circuited or open-circuited and are excluded [36] We defined the maximum of the Gaussian distribution, fitted to the histograms, as the representative current level of each state, as shown in Figure 4.3b. In Figures 4.3c and 4.3d, the two-dimensional *J-V* histograms are depicted as contour plots for all the working open and closed state junctions, respectively. Although the variance of the current level in the open

state is larger than that in the closed state, we find that the current levels of the two different states are separated by two orders of magnitude. This means that the molecular junctions with the MLG top electrode show distinct electrical properties in response to the light, similar to previous reports [25].

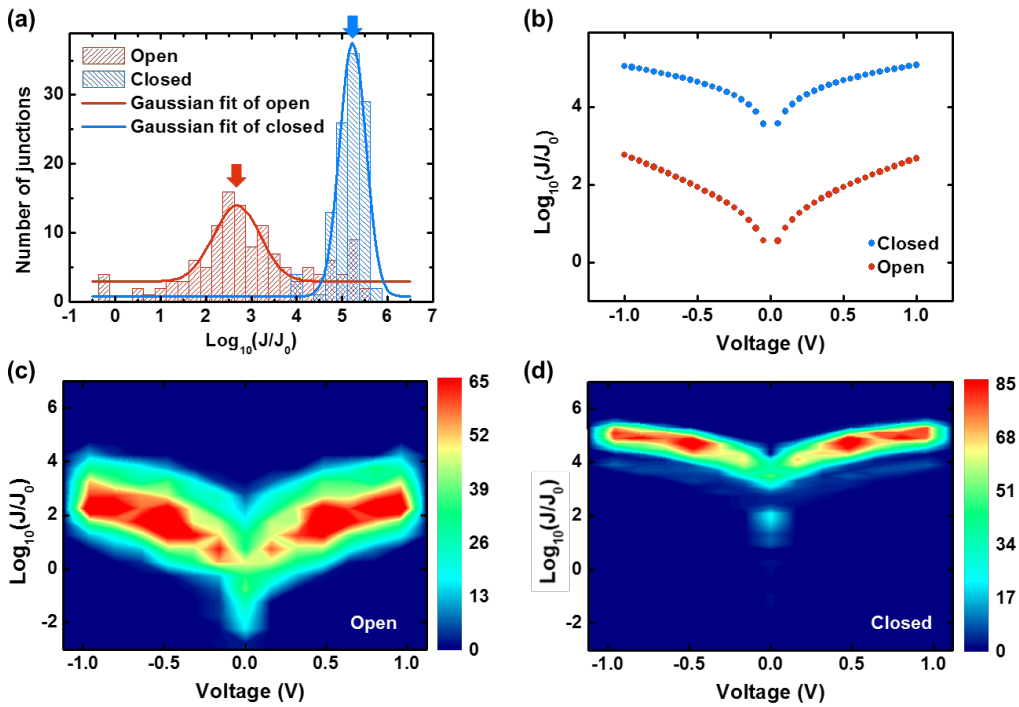

Figure 4.3. (a) Histogram of current-density values for all open- and closed-state molecular junctions measured at a bias of $V = 1$ V. (b) Representative logarithmic *J-V* curves for the closed and open state DAE molecular junctions. (c,d) Two-dimensional logarithmic *J-V* plots for intact molecular junctions in (c) open and (d) closed states. Here, $J_0 = 1$ A/cm^2 (see the text).

Subsequently, we examined the phototransition properties of the DAE molecular junctions. Figure 4a shows real-time current density (*J-t*) measurements for three cases: open state in the dark (black line), open state exposed to 15 mW UV light (purple line),

and closed state exposed to visible light (green line) with the same intensity as the UV light.

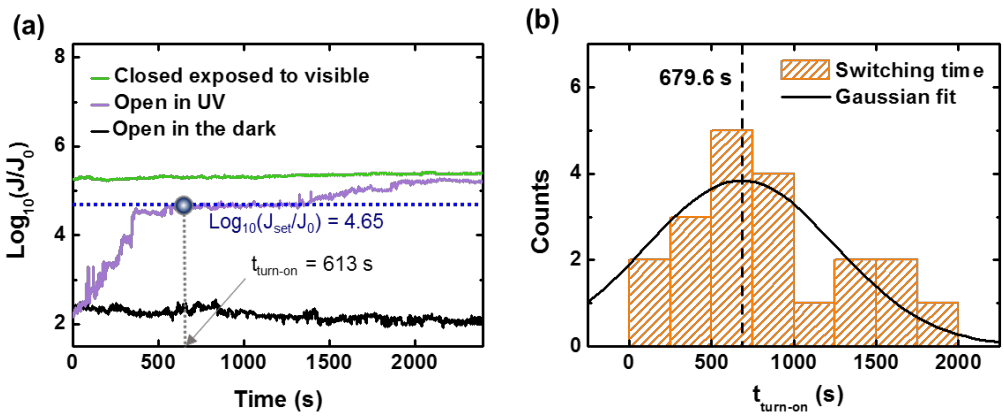

Figure 4.4. (a) Real-time measurement of the current density for each state with or without exposure to light at an applied bias voltage of V = 1 V. The switching time ($t_{\text{turn-on}}$) is indicted by an arrow. (b) Histogram for the measured switching time required to transition from the open to the closed state. The Gaussian fit to the histogram is shown by the solid line, and the average switching time is shown by the dashed line.

All the measurements were carried out under a constant voltage of 1 V, and the time on the x-axis of the graph was adjusted to start from the point when irradiation was initiated. The current level of the junction in the open state in the dark showed no changes, which suggests that the bias voltage applied to the molecular junction cannot induce the switching. In addition, for the case of the molecular junction prepared in the closed state, the switching behavior could not be observed when exposed to visible light. On the other hand, we observed a unidirectional real-time switching behavior from the open to the closed state under UV light illumination. The switching time of the representative molecular junction for the open state to transition to the closed state upon exposure to UV light was found to be 613 s (indicated as $t_{turn\text{-}on}$ in Figure 4.4a).

Figure 4.5 shows real-time measurement data for 20 molecular junctions in the open state, which were changed to the closed state by illuminating with UV light. All data was adjusted to start from the point, when the UV light was irradiated. The light was shined in for a sufficiently long time until the current density remained constant. The intensity of the UV light used was 15 mW. We define the switching time as the time to reach $\log_{10}(J_{set}/J_0)$ = 4.65, where J_{set} is 90% of the average current density of the molecular junctions in the closed state. The switching times obtained from 21 different molecular junctions were distributed as shown in Figure 4.4b. The average switching time for these 21 molecular junctions was determined to be around 680 s by performing a Gaussian fit to the statistical data.

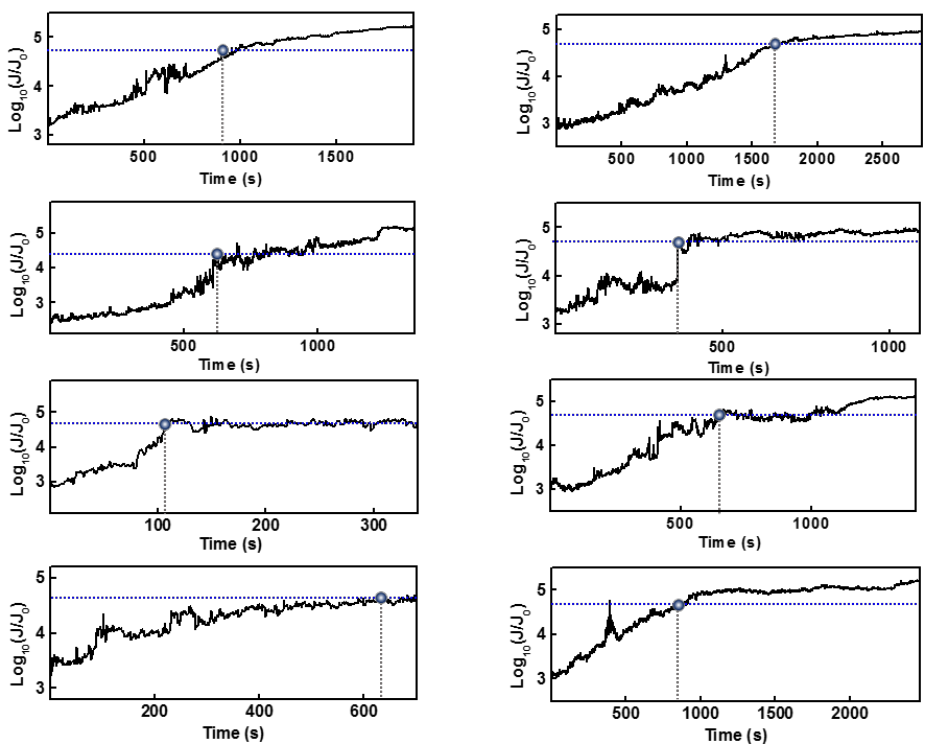

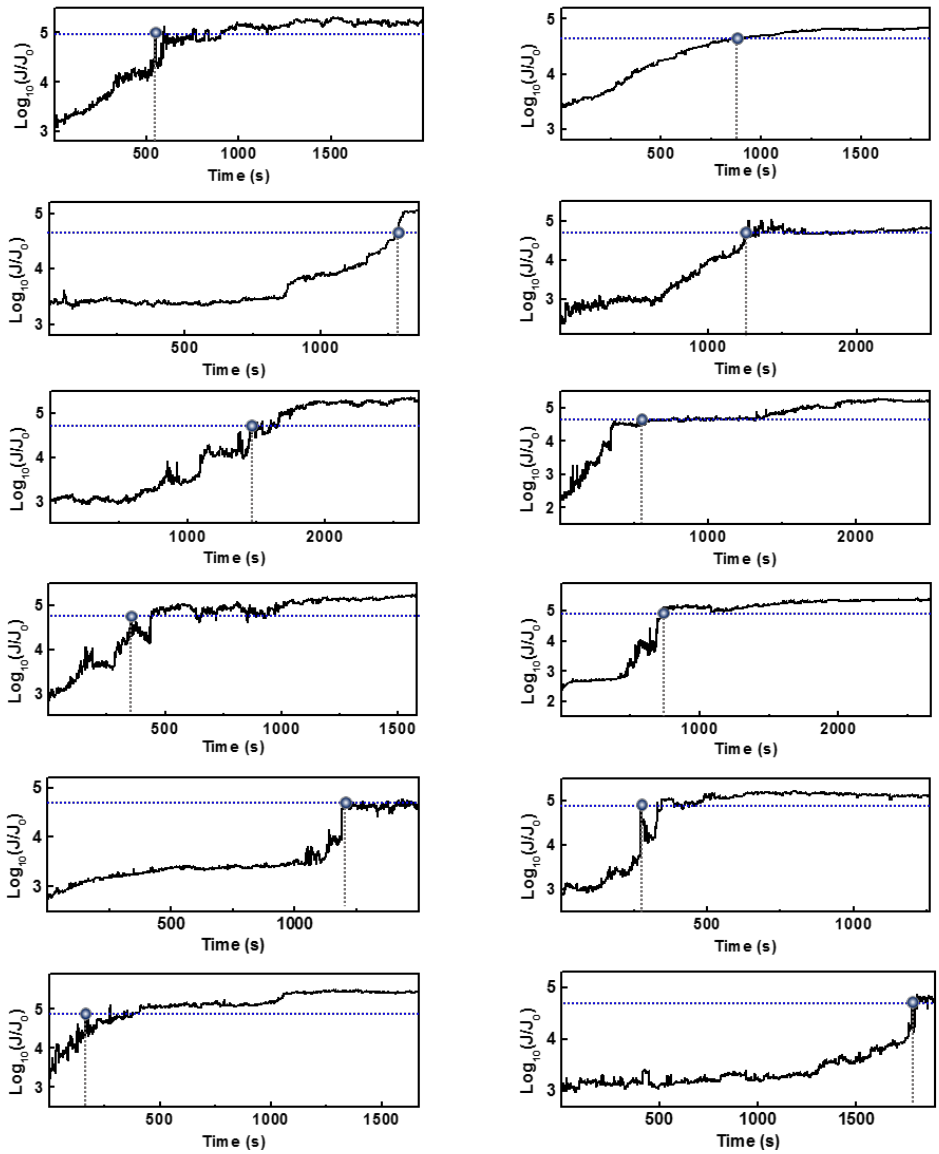

Figure 4.5. Real-time measurement of switching from the open state to the closed state, when molecular junctions are illuminated with UV light. Set currents and extracted switching times are marked in the plots. 1 V bias was applied in all the cases.

3.3 Theoretical Interpretation of the Charge Transport for MLG-DAE junction

Note that the photoswitching is intrinsically due to the UV-responsive reaction of the core of the DAE molecules. From irradiation experiments on a thiophene-derived DAE in solution the irreversible formation of a non-photoactive byproduct is known [37]. Such process could reduce the number of available fully functional molecular switches somewhat, but it would not render the whole device non-functional. However, during irradiation of our furan-bearing DAEs in solution a similar fatigue mechanism was never observed.

To gain a better understanding of the charge transport through the molecular junctions and to investigate the unidirectional switching behavior, we apply the Landauer formalism [38]. We approximate the current through an equivalent single-molecule junction as

$$I_{\text{single}} = \frac{c}{NA} I_{\text{exp}} = \frac{2e}{h} \int_{-\infty}^{\infty} T(E)[f_1(E) - f_2(E)]dE \quad . \tag{2}$$

In Eq. (1), $f_X(E) = (1 + \exp((E - \mu_X)/k_{\text{B}}T))^{-1}$ is the Fermi-Dirac distribution function, where μ_X is the chemical potential of the electrode X = top or bottom, and $T(E)$ is the transmission function with a Lorentzian shape around the molecular orbital (MO) n described as

$$T(E) = \sum_n \frac{4\Gamma_{n,\text{top}}\Gamma_{n,\text{bottom}}}{[\Gamma_n{}^2 + (E - E_n)^2]}. \tag{2}$$

Here $\Gamma_{n,X}$ indicates the electronic coupling strength of the MO n to the respective electrode X, and $\Gamma_n = \Gamma_{n,\text{top}} + \Gamma_{n,\text{bottom}}$ defines the total linewidth broadening. Counting all energies from the Fermi energy E_{F} as the reference, E_n is the difference between the eigenenergy of the MO and the Fermi energy of the electrodes $\mu_X \approx E_{\text{F}}$.

Since our system consists of many molecules, we calculate the current per molecule I_{single} by dividing the experimentally measured current I_{exp} by the number of molecules *NA* in the junction. Here, we choose the coverage *N* as 4.4×10^{14} cm^{-2} and 5.4×10^{14} cm^{-2} for the closed-state and open-state DAE, respectively [24]. The reason why the packing density of the closed state is lower than those of the open state is because the energetically most favorable packing and tilt angle (i.e., the optimized molecular conformations that minimize the free energy) are different for the closed state and the open state [24] The contact area *A* of the molecular junctions is estimated to be equal to the geometric hole size of 314 μm^2. Furthermore, we multiplied the current by a phenomenological factor c = 3000, because the current per molecule in SAMs has been found to be about 3000 times lower than that in a single-molecule junction in the case of a conjugated molecular wire [39]. This effect is attributed to the fact that SAMs are more effectively screening the external electric field and provide more paths for molecular heat dissipation as compared to single-molecule junctions. These factors facilitate the tunneling through a single-molecule junction as compared to the SAM system. Finally, since the number of molecules that make electrical contact with both electrodes in large-scale molecular junctions is only a fraction of the total number of molecules, per molecule the contact is less conductive than a single-molecule junction [40].

Let us point out that we expect various defects in our experimental devices that cannot be controlled perfectly. For example, polymer residues, ripples, cracks or voids on or in the CVD-grown MLG film will influence the effective contact area with the SAM [41-42]. Similarly, defects at the bottom electrode resulting from grain boundaries or photoresist residues may cause an irregular arrangement of molecules. Consequently, the actual contact area will be altered and distances between the molecules and electrodes will

vary [43-44]. Considering these factors, the contact area and the distance between the SAM and the MLG can neither be accurately predicted nor measured.

To simplify the analysis of I_{single}, we introduce the following assumptions: (i) The contribution from a single MO n=0 determines the current [21, 38]. (ii) Since the experimental *J-V* characteristics are almost symmetric with regard to bias polarity, we assume that the coupling strength is symmetric, i.e., $\Gamma = \Gamma_{0,top} + \Gamma_{0,bottom}$ and $\Gamma_{0,top} = \Gamma_{0,bottom}$ [45]. (iii) The energy level E_0 of the SAM system is fixed, when a bias voltage is applied between the two electrodes [38, 45-46]. By adopting these assumptions, Equation (2) reduces to

$$T(E) = \frac{\Gamma^2}{[\Gamma^2+(E-E_0)^2]}, \quad (3)$$

where the charge injection barrier is given as $E_0 = E_{\mathrm{HOMO}} - E_{\mathrm{F}}$ or $E_0 = E_{\mathrm{LUMO}} - E_F$ with E_{HOMO} and E_{LUMO} being the energy level of the highest occupied molecular orbital (HOMO) and the lowest unoccupied molecular orbital (LUMO), respectively.

Let us note that with all these approximations, we use a very simple model to analyze the charge transport through the complex Au-DAE-MLG systems. Indeed the symmetric single-level model appears to be oversimplified, given that junctions are structurally asymmetric. Thus, we expect that the DAE molecules exhibit a weak physical contact to MLG and a strong covalent bond to Au, making it necessary to distinguish between the two couplings $\Gamma_{0,bottom}$ and $\Gamma_{0,top}$. However, the couplings also significantly depend on the intramolecular coupling strength between the central part of the molecule and the contact groups at the ends [47]. Indeed, Nijhuis and collaborators showed that both *J-V* curves as well as $\Gamma_{0,bottom}$ and $\Gamma_{0,top}$ are almost symmetric for ferrocenyl-based molecules between one covalently bound and one physisorbed contact, when the ferrocenyl unit was located at the

center of the molecule [48] We therefore hope that the effective parameters Γ and E_0, extracted from the single-level model, yield meaningful trends. Let us also point out that only the absolute value of E_0, i.e. $|E_0|$, can be determined from current-voltage characteristics. To simplify the notation, we will omit the symbol for the absolute value in the following, and assume that $E_0 \geq 0$.

As described in a previous publication [38], we have numerically fitted experimental I_{single}–V curves to estimate Γ and E_0 values by adopting the Levenberg-Marquardt algorithm. Figures 4.6a and 5b show representative I_{single}–V curves and the corresponding fits for the closed and open states. The fits reproduce the measurements well with minimal variation over the whole voltage range. In addition, we conducted the fitting for 91 closed-state and 84 open-state molecular junctions, and then extracted Γ and E_0 values for all the junctions. All the Γ and E_0 values determined are presented in the scatter plot in Figures 4.6c and 4.6d. By averaging these distributions, the effective coupling strength Γ for closed and open states was determined to be 1.93 ± 0.12 meV and 0.0572 ± 0.0072 meV, respectively, and the corresponding charge injection barrier E_0 for closed and open states was extracted to be 1.560 ± 0.054 meV and 0.756 ± 0.012 meV, respectively, as summarized in Table 4.1. Figures 4.7e and 4.7f show schematic illustrations of junction structures for closed- and open-state molecular junctions, where we have visualized the coupling strength Γ between the molecule and the electrodes by arrows of different size. Note that the level alignment E_0 shows a complex behavior opposite to the naive expectation that E_0 in the open state would be higher than for the closed state. This expectation is based on the fact that the electronic gap between the HOMO and the LUMO in an isolated DAE molecule is larger in the open state than in the closed one.

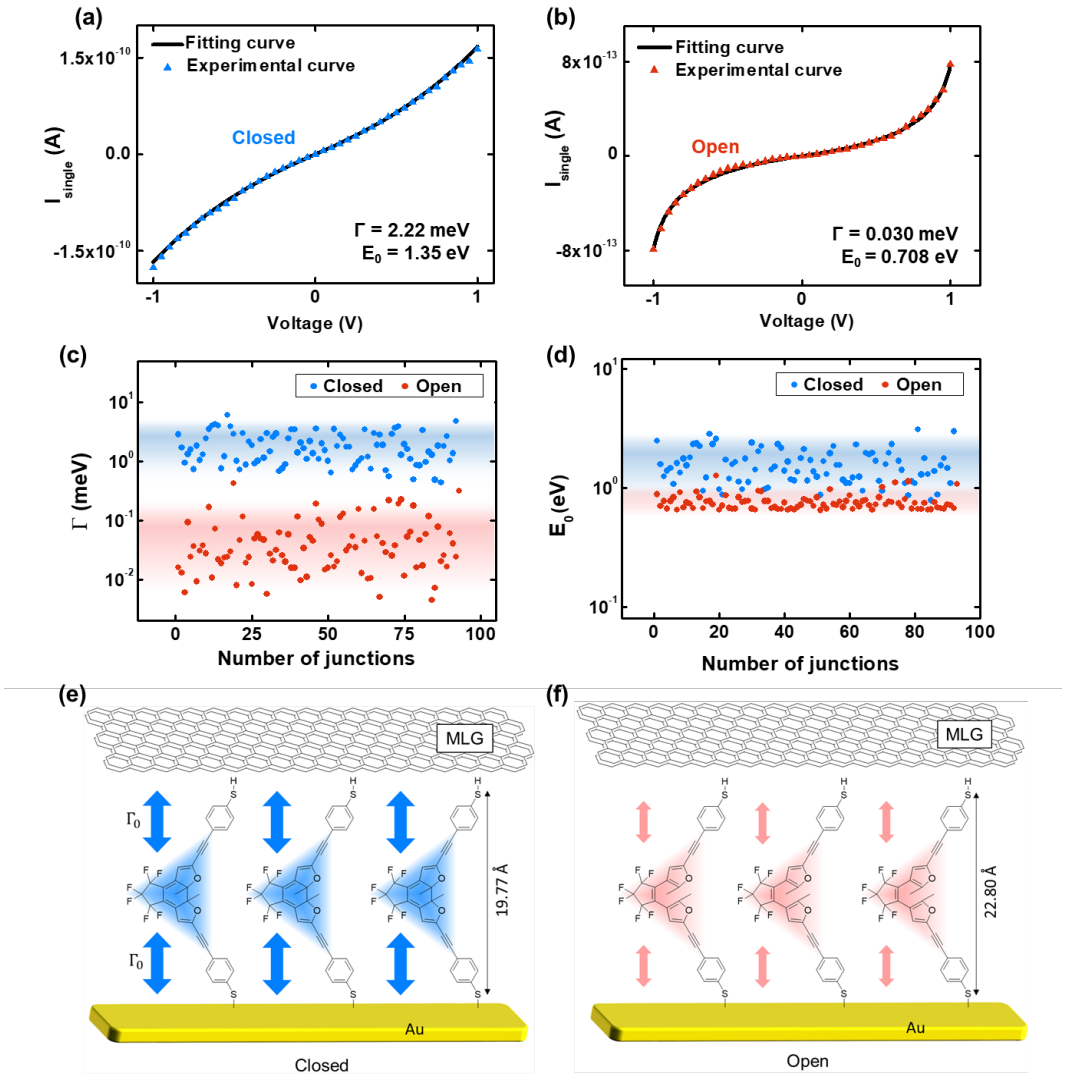

Figure 4.6. (a,b) A representative I_{single}-V curve measured for the (a) closed and (b) open state, with the fitting curve (shown as a solid line) calculated based on the Landauer formula. The corresponding coupling and level alignment values used in the fits are listed at the bottom right of each graph. (c,d) Scatter point plots for (c) Γ and (d) E_0 values for intact molecular junctions in the closed and open state. The shaded regions represent areas, where the data points deviate by no more than 60% from the averages. Here, Γ values for the closed and open states are clearly separated from each other, while they mix for E_0. (e,f) Schematic illustration of junction structures for the (e) closed and (f) open state. The coupling strength between molecules and the electrodes Γ is indicated by the size of the arrow.

		Γ (meV)	E_0 (eV)
Au – DAE - MLG	Closed	1.93 ± 0.12	1.560 ± 0.054
	Open	0.0572 ± 0.0072	0.756 ± 0.012
Au – DAE - rGO	Closed	0.462± 0.039	2.19 ± 0.18
	Open	0.250 ± 0.040	2.72 ± 0.38

Table 4.1. Charge injection barrier (E_0) and coupling constant (Γ) as extracted from a set of I_{single}–V curves by using the Landauer formula.

Closed			
Method	HOMO (eV)	LUMO (eV)	Gap (eV)
DFT (PBE)	-4.57	-3.50	1.07
G_0W_0	-6.00	-0.40	5.60
evGW	-6.17	-1.97	4.20
ΔSCF	-6.02	-2.13	3.89
Open			
Method	HOMO (eV)	LUMO (eV)	Gap (eV)
DFT (PBE)	-5.03	-2.74	2.29
G_0W_0	-6.76	-1.01	5.75
evGW	-7.07	-0.46	6.61
ΔSCF	-6.32	-1.27	5.05

Table 4.2. Energies of HOMO and LUMO states in open and closed configurations of the isolated molecules in vacuum and resulting electronic gap.

Calculations using various levels of ab-initio electronic structure theory are summarized in Table 4.2. They have been carried out with the help of the program package TURBOMOLE [49] As a first method, we have chosen density functional theory (DFT) together with PBE [50-52] as exchange-correlation functional. Since the DFT typically underestimates quasiparticle gaps substantially by some eV [53], we have computed them also with ΔSCF [53], G_0W_0 [54], and eigenvalue self-consistent GW (evGW) [55].

All of these calculations show that the HOMO-LUMO gap of DAE decreases, when being switched from the open to the closed state. This confirms the assertion made in the previous paragraph and matches well with the picture of more delocalized electrons in the closed state. Indeed both HOMO and LUMO wavefunctions in the closed state spread more strongly over the hole molecule than in the open one, as it is visible in Figure 4.7. It is also apparent from the expression for the transmission in Equation (3) that the difference in Γ values between closed and open states determines the magnitude of current rather than the difference in E_0 values. In particular, it is notable that the effective value of Γ in the closed state is more than 30 times larger than that of the open state, while E_0 differs only by a factor of around 2. Thus, the Γ values explain, why the closed state is more conductive than the open one.

In addition to a previous explanation that the small quantum yield of the ring opening reaction reduces the switching rate [20], the relatively strong coupling between DAE and MLG electrodes in the closed state may also cause the unidirectional switching. It is possible that the strong interaction between the closed state of the DAE molecules and the electrode can quench the photoexcited closed state, effectively disturbing the switching process and eventually preventing the transition to the open state [17, 56-57].

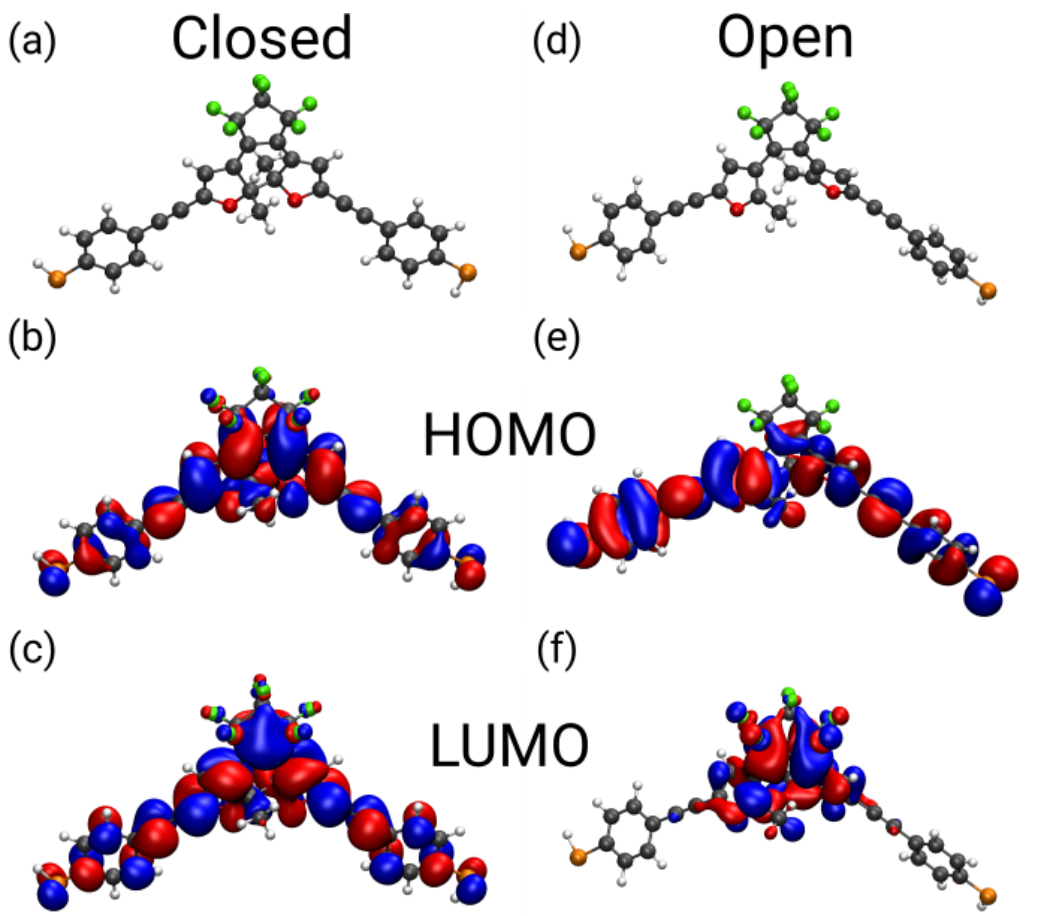

Figure 4.7. (a) Equilibrium geometry of the DAE molecule in the gas phase in its closed state, and corresponding (b) HOMO and (c) LUMO wavefunctions. (d-f) The same for the open state.

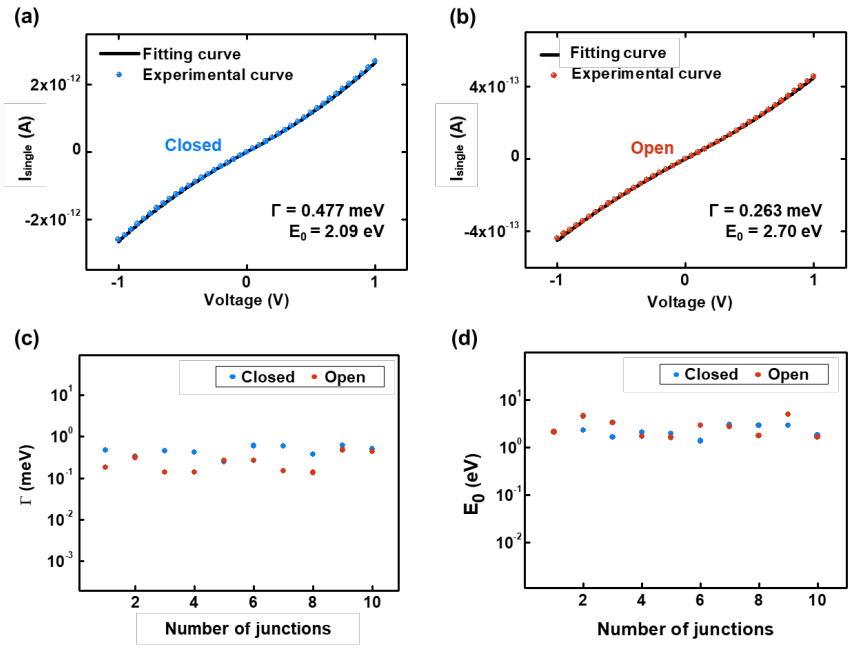

Figure 4.8. Representative I_{single}-V curves measured for the (a) closed and (b) open state of Au-DAE-rGO junctions and corresponding fitting curves. The coupling value and charge injection barrier for the I_{single}-V curves are shown at the bottom right of each graph. Scatter point plots of (c) Γ and (d) E_0 values for closed and open states of Au-DAE-rGO junctions.

We also applied the same method to analyze the measurement data for Au-DAE-rGO junctions (Figure 4.8, Supporting Information) reported in our previous work [25]. In Figures 4.8a and 4.8b, representative fitting results are shown for closed and open states, both of which were well-fitted. The averaged fitting results, obtained from 10 Au-DAE-rGO junctions, are given in Table 4.1. The extracted Γ values for closed and open states were calculated as 0.462 ± 0.039 meV and 0.250 ± 0.040 meV, respectively, both of which are roughly one order lower than the value obtained for the closed state in Au-DAE-MLG junctions. The effective E_0 values for closed and open states were found to be 2.19 ± 0.18 meV and 2.72 ± 0.38 meV, respectively. As depicted in Figure 4.8c, the distribution of Γ values for both states in Au-DAE-rGO junctions is in a similar range

within one order, in contrast to the Au-DAE-MLG junctions which showed a significant difference in electronic couplings between closed and open states. Level alignments E_0 between open and closed junctions in Fig. S8d practically do not differ. This result corroborates that bidirectional switching in Au-DAE-rGO junctions correlates well with similar and small Γ values for both closed and open states.

The HOMO-LUMO gaps determined with ΔSCF, G_0W_0 and evGW in Table 4.1 are expected to be more reliable than those of DFT [53], and we find indeed that they are much larger than the predictions of DFT. Let us point out that the quasiparticle electronic gap values can provide bounds for the level alignment E_0, used in the fits with the single-level model. In particular, it should be less than half of the gap size, $E_0 \leq \Delta/2$, since screening effects inside the junctions due to the presence of the electrodes and other molecules are expected to reduce the effective electronic gap. While the bandgap values obtained from ΔSCF, G_0W_0 and evGW are compatible with the experimental values for E_0 from Au-DAE-MLG and Au-DAE-rGO junctions in open and closed states, DFT clearly violates the approximate relation $E_0 \leq \Delta/2$.

The different tendency of the Γ values in the Au-DAE-MLG junctions compared to those in the Au-DAE-rGO junctions can reasonably explain, why the former junctions show unidirectional switching, whereas the latter exhibit bidirectional switching. Our analysis reveals that the interaction between the molecules and the electrodes is important not only for the overall current level but also for the directionality of the switching behavior. We conclude that the interaction between the DAE molecules and different electrode materials can lead to drastically different device characteristics.

4.4. Conclusion

In summary, we fabricated and characterized DAE photoswitching molecular junctions using Au bottom and MLG top electrodes. We found clearly distinguishable electrical properties for the molecular junctions between closed and open states with average current levels differing by two orders of magnitude. At the same time we found in real-time measurements that the junctions exhibited a unidirectional switching behavior from the open to the closed state. To better understand the unidirectionality, we extracted electronic coupling and level alignment parameters, Γ and E_0, by fitting experimental *J-V* curves with the Landauer formula. The calculated Γ value for the Au-DAE-MLG junctions in the closed state was significantly larger than in the open state. A comparison with previously measured Au-DAE-rGO junctions, which show bidirectional switching, revealed that the electronic couplings Γ correlate well with the photoswitching behavior and not the level alignment. By relating the electronic measurements with photoswitching device characteristics, we thus attribute the inability to switch to the open state to the strong coupling between DAE and the MLG electrode in the closed state together with the low quantum yield of the opening reaction. Our study suggests that the electronic coupling between molecules and electrodes plays a significant role for any molecular photoswitching device.

References

(1) Bumm, L. A.; Arnold, J. J.; Cygan, M. T.; Dunbar, T. D.; Burgin, T. P.; Jones, L.; Allara, D. L.; Tour, J. M.; Weiss, P. S., *Science* **1996,** *271*, 1705-1707.

(2) Wold, D. J.; Haag, R.; Rampi, M. A.; Frisbie, C. D., *J. Phys. Chem. B* **2002,** *106*, 2813-2816.

(3) Tanaka, T.; Osuka, A., *Chem. Soc. Rev.* **2015,** *44*, 943-969.

(4) Aviram, A.; Ratner, M. A., *Chem. Phys. Lett.* **1974,** *29*, 277-283.

(5) Chen, X.; Roemer, M.; Yuan, L.; Du, W.; Thompson, D.; del Barco, E.; Nijhuis, C. A., *Nat. Nanotechnol.* **2017,** *12*, 797-803.

(6) Osorio, E. A.; Moth-Poulsen, K.; van der Zant, H. S. J.; Paaske, J.; Hedegård, P.; Flensberg, K.; Bendix, J.; Bjørnholm, T., *Nano Lett.* **2009,** *10*, 105-110.

(7) Jia, C.; Migliore, A.; Xin, N.; Huang, S.; Wang, J.; Yang, Q.; Wang, S.; Chen, H.; Wang, D.; Feng, B.; Liu, Z.; Zhang, G.; Qu, D.-H.; Tian, H.; Ratner, M. A.; Xu, H. Q.; Nitzan, A.; Guo, X., *Science* **2016,** *352*, 1443-1445.

(8) Song, H.; Kim, Y.; Jang, Y. H.; Jeong, H.; Reed, M. A.; Lee, T., *Nature* **2009,** *462*, 1039-1043.

(9) Capozzi, B.; Chen, Q.; Darancet, P.; Kotiuga, M.; Buzzeo, M.; Neaton, J. B.; Nuckolls, C.; Venkataraman, L., *Nano Lett.* **2014,** *14*, 1400-1404.

(10) Cui, L.; Miao, R.; Wang, K.; Thompson, D.; Zotti, L. A.; Cuevas, J. C.; Meyhofer, E.; Reddy, P., *Nat. Nanotechnol.* **2018,** *13*, 122-127.

(11) Seo, S.; Min, M.; Lee, S. M.; Lee, H., *Nat. Commun.* **2013,** *4*, 1920.

(12) Hagen, S.; Leyssner, F.; Nandi, D.; Wolf, M.; Tegeder, P., *Chem. Phys. Lett.* **2007,** *444*, 85-90.

(13) Alemani, M.; Peters, M. V.; Hecht, S.; Rieder, K.-H.; Moresco, F.; Grill, L., *J. Am. Chem. Soc.* **2006,** *128*, 14446-14447.

(14) Irie, M.; Kobatake, S.; Horichi, M., *Science* **2001,** *291*, 1769-1772.

(15) Whalley, A. C.; Steigerwald, M. L.; Guo, X.; Nuckolls, C., *J. Am. Chem. Soc.* **2007,** *129*, 12590-12591.

(16) Kim, D.; Jeong, H.; Lee, H.; Hwang, W. T.; Wolf, J.; Scheer, E.; Huhn, T.; Jeong, H.; Lee, T., *Adv. Mater.* **2014,** *26*, 3968-3973.

(17) Dulic, D.; van der Molen, S. J.; Kudernac, T.; Jonkman, H. T.; de Jong, J. J.; Bowden, T. N.; van Esch, J.; Feringa, B. L.; van Wees, B. J., *Phys. Rev. Lett.* **2003,** *91*, 207402.

(18) Zhuang, M.; Ernzerhof, M., *J. Chem. Phys.* **2009,** *130*, 114704.

(19) Zhuang, M.; Ernzerhof, M., *Phys. Rev. B* **2005,** *72*, 073104.

(20) Sendler, T.; Luka-Guth, K.; Wieser, M.; Wolf, J.; Helm, M.; Gemming, S.; Kerbusch, J.; Scheer, E.; Huhn, T.; Erbe, A., *Adv. Sci.* **2015,** *2*, 1500017.

(21) Jia, C.; Wang, J.; Yao, C.; Cao, Y.; Zhong, Y.; Liu, Z.; Liu, Z.; Guo, X., *Angew. Chem., Int. Ed. Engl.* **2013,** *52*, 8666-8670.

(22) van der Molen, S. J.; Liao, J.; Kudernac, T.; Agustsson, J. S.; Bernard, L.; Calame, M.; van Wees, B. J.; Feringa, B. L.; Schönenberger, C., *Nano Lett.* **2008,** *9*, 76-80.

(23) Zotti, L. A.; Kirchner, T.; Cuevas, J. C.; Pauly, F.; Huhn, T.; Scheer, E.; Erbe, A., *Small* **2010,** *6*, 1529-1535.

(24) Kronemeijer, A. J.; Akkerman, H. B.; Kudernac, T.; van Wees, B. J.; Feringa, B. L.; Blom, P. W. M.; de Boer, B., *Adv. Mater.* **2008,** *20*, 1467-1473.

(25) Kim, D.; Jeong, H.; Hwang, W.-T.; Jang, Y.; Sysoiev, D.; Scheer, E.; Huhn, T.; Min, M.; Lee, H.; Lee, T., *Adv. Funct. Mater.* **2015,** *25*, 5918-5923.

(26) Reina, A.; Jia, X.; Ho, J.; Nezich, D.; Son, H.; Bulovic, V.; Dresselhaus, M. S.; Kong, J., *Nano Lett.* **2008,** *9*, 30-35.

(27) Chae, S. J.; Güneş, F.; Kim, K. K.; Kim, E. S.; Han, G. H.; Kim, S. M.; Shin, H. J.; Yoon, S. M.; Choi, J. Y.; Park, M. H.; Yang, C. W.; Pribat, D.; Lee, Y. H., *Adv. Mater.* **2009,** *21*, 2328-2333.

(28) Sun, Z.; Yan, Z.; Yao, J.; Beitler, E.; Zhu, Y.; Tour, J. M., *Nature* **2010,** *468*, 549-552.

(29) Li, X.; Cai, W.; An, J.; Kim, S.; Nah, J.; Yang, D.; Piner, R.; Velamakanni, A.; Jung, I.; Tutuc, E.; Sanjay, K. B.; Luigi, C.; Rodney, S. R., *Science* **2009,** *324*, 1312-1314.

(30) Kim, K. S.; Zhao, Y.; Jang, H.; Lee, S. Y.; Kim, J. M.; Kim, K. S.; Ahn, J.-H.; Kim, P.; Choi, J.-Y.; Hong, B. H., *Nature* **2009,** *457*, 706-710.

(31) Jo, G.; Choe, M.; Cho, C. Y.; Kim, J. H.; Park, W.; Lee, S.; Hong, W. K.; Kim, T. W.; Park, S. J.; Hong, B. H.; Kahng, Y. H.; Lee, T., *Nanotechnol.* **2010,** *21*, 175201.

(32) Jang, Y.; Kwon, S.-J.; Shin, J.; Jeong, H.; Hwang, W.-T.; Kim, J.; Koo, J.; Ko, T.; Ryu, S.; Wang, G., *ACS Appl. Mater. Interfaces* **2017,** *9*, 42043-42049.

(33) Kim, J.; Jeong, H.; Seong, S.; Kim, M.; Kim, D.; Hwang, W.-T.; Jang, Y.; Choi, B. Y.; Koo, J.; Park, S. B.; Noh, J.; Lee, T., *Curr. Appl. Phys.* **2017,** *17*, 1459-1464.

(34) Snegir, S.; Mukha, I.; Sysoiev, D.; Lacaze, E.; Huhn, T.; Pluchery, O., *Materialwiss. Werkstofftech.* **2016,** *47*, 229-236.

(35) Cho, C.-Y.; Choe, M.; Lee, S.-J.; Hong, S.-H.; Lee, T.; Lim, W.; Kim, S.-T.; Park, S.-J., *J. Appl. Phys.* **2013,** *113*, 113102.

(36) Kim, T. W.; Wang, G. N.; Lee, H.; Lee, T., Statistical Analysis of Electronic Properties of Alkanethiols in Metal-Molecule-Metal Junctions. *Nanotechnol.* **2007,** *18*, 315204.

(37) Higashiguchi, K.; Matsuda, K.; Kobatake, S.; Yamada, T.; Kawai, T.; Irie, M., *Bull. Chem. Soc. Jpn.* **2000,** *73*, 2389-2394.

(38) Kim, Y.; Hellmuth, T. J.; Sysoiev, D.; Pauly, F.; Pietsch, T.; Wolf, J.; Erbe, A.; Huhn, T.; Groth, U.; Steiner, U. E.; Scheer, E., *Nano Lett.* **2012,** *12*, 3736-3742.

(39) Selzer, Y.; Cai, L.; Cabassi, M. A.; Yao, Y.; Tour, J. M.; Mayer, T. S.; Allara, D. L., *Nano Lett.* **2005,** *5*, 61-65.

(40) Li, B.; Famili, M.; Pensa, E.; Grace, I. M.; Long, N. J.; Lambert, C.; Albrecht, T.; Cohen, L. F., *Nanoscale* **2018,** *10*, 19791-19798.

(41) Liu, N.; Pan, Z.; Fu, L.; Zhang, C.; Dai, B.; Liu, Z., *Nano Research* **2011,** *4*, 996-1004.

(42) Chen, X.; Zhang, L.; Chen, S., *Synth. Met.* **2015,** *210*, 95-108.

(43) Jeong, H.; Hwang, W. T.; Kim, P.; Kim, D.; Jang, Y.; Min, M.; Xiang, D.; Song, H.; Park, Y. D.; Jeong, H.; Lee, T., *Appl. Phys. Lett.* **2015,** *106*, 063110.

(44) Yuan, L.; Jiang, L.; Zhang, B.; Nijhuis, C. A., *Angew. Chem. Int. Ed.* **2014,** *53*, 3377-3381.

(45) Scheer, E.; Cuevas, J. C., *Molecular Electronics: An Introduction to Theory and Experiment*. World Scientific: **2010**; Chapter 13, pp 364-366.

(46) Briechle, B. M.; Kim, Y.; Ehrenreich, P.; Erbe, A.; Sysoiev, D.; Huhn, T.; Groth, U.; Scheer, E., *Beilstein J. Nanotechnol.* **2012,** *3*, 798-808.

(47) Moth-Poulsen, K.; Bjørnholm, T., *Nat. Nanotechnol.* **2009,** *4*, 551-556.

(48) Yuan, L.; Nerngchamnong, N.; Cao, L.; Hamoudi, H.; Del Barco, E.; Roemer, M.; Sriramula, R. K.; Thompson, D.; Nijhuis, C. A., *Nat. Commun.* **2015,** *6*, 6324.

(49) TURBOMOLE V7.3, a development of University of Karlsruhe and Forschungszentrum Karlsruhe GmbH, 1989-2007, TURBOMOLE GmbH, since 2007; available from http://www.turbomole.com.

(50) Perdew, J. P.; Wang, Y., *Phys. Rev. B* **1992,** *45*, 13244-13249.

(51) Perdew, J. P.; Burke, K.; Wang, Y., *Phys. Rev. B* **1996,** *54*, 16533-16539.

(52) Perdew, J. P.; Burke, K.; Ernzerhof, M., *Physi. Rev. Lett.* **1996,** *77*, 3865-3868.

(53) Martin, R. M., *Electronic Structure: Basic Theory and Practical Methods*. Cambridge University Press: **2004**.

(54) van Setten, M. J.; Weigend, F.; Evers, F., *J. Chem. Theory Comput.* **2012,** *9*, 232-246.

(55) Kaplan, F.; Harding, M. E.; Seiler, C.; Weigend, F.; Evers, F.; van Setten, M. J., *J. Chem. Theory Comput.* **2016,** *12*, 2528-2541.

(56) Comstock, M. J.; Levy, N.; Kirakosian, A.; Cho, J.; Lauterwasser, F.; Harvey, J. H.; Strubbe, D. A.; Fréchet, J. M. J.; Trauner, D.; Louie, S. G.; Crommie, M. F., *Phys. Rev. Lett.* **2007,** *99*, 038301.

(57) Gahl, C.; Schmidt, R.; Brete, D.; McNellis, E. R.; Freyer, W.; Carley, R.; Reuter, K.; Weinelt, M., *J. Am. Chem. Soc.* **2010,** *132*, 1831-1838.

Chapter 5. Summary

In this thesis, I described the research results mainly focusing on the electrical and photoswitching characterization of the large-area molecaular monolayer junctinos with graphene electrode. The main chapters were devoted to electrical properties of benzenedithiolate and DAE molecular junctions with CVD-grown multilayer graphene.

First, I investigated the charge transport behaviors from in length- and temperature-dependent analyses. I demonstrated that the primary charge transport of our molecular junctions is non-resonant tunneling. Then I also fabricated the same molecular devices on flexible substrates. The reliability of flexible molecular electronic devices was examined under various mechanical bending conditions. The electrical characteristics of the devices were well maintained in all tested bending environments. For the last, I performed inelastic electron tunneling spectroscopy (IETS) measurement experiments with graphene-interlayer molecular junctions. I observed obvious IETS signals indicating unique vibration modes of molecules, which consist with previously known values. The existence of benzenethiolate molecule as an active device component in graphene-interlayer molecular junctions has been explicitly identified.

And secondly, I fabricated molecular junctions consisting of self-assembled monolayers of BDT with p-doped multi-layer graphene electrode. The p-type doping of graphene film was done by treating pristine graphene (work function of ~4.40 eV) with TFMS acid, resulting increased work function (~5.23 eV). The p-doped graphene-electrode molecular junctions statistically showed an order of magnitude higher current density and lower charge injection barrier height than those of pristine graphene-electrode molecular junctions, as a result of interface engineering. This enhancement is due to increased work

function of TFMS-treated p-doped graphene electrode in highest occupied molecular orbital-mediated tunneling molecular junctions. The validity of these results was proven by theoretical analysis based on coherent transport model considering asymmetric couplings at electrode-molecule interfaces.

In chapter 4, I fabricated and characterized vertical molecular junctions consisting of self-assembled monolayers (SAMs) of diarylethene (DAE) contacted by a multilayer graphene (MLG) electrode on the top and gold on the bottom. The DAE molecular junctions show two stable electrical states, a closed state (high conductance) or an open state (low conductance), which are created upon illumination with UV or visible light, respectively. For the Au-DAE-MLG junction structure, we observe that the current levels between the two conductance states are separated by two orders of magnitude. However, in a real-time, I observed only unidirectional switching behavior from the open to the closed state. I interpreted this phenomenon with strong electrode-molecule coupling with Landauer formula.

국문초록

그래핀 전극 기반 대면적 단분자박막 분자 접합의 전기적 특성 및 광스위칭 현상에 대한 연구

장연식

서울대학교 물리천문학부

분자전자학은 단일 분자 또는 자기조립단분자박막을 정류기, 트랜지스터, 스위치, 메모리, 회로 등과 같은 전자 소자의 핵심 구성 요소로 사용하고자 하는 연구 분야이다. 분자 전자학은 기존 실리콘 기반 전자 소자의 한계를 뛰어 넘는 궁극적인 소형화에 도달하는 것을 목표로 하며, 저비용, 높은 집적도 및 간단한 합성 공정, 단분자를 빌딩 블록으로 사용할 수 있는 이점을 가지고 있다. 그러나 낮은 소자 안정성, 신뢰성 및 재현성으로 인해 분자 전자학에는 많은 해결 과제가 산적해 있다. 또한, 분자 접합에서의 전하 수송 특성 및 전극-금속 계면 특성이 완전히 이해되지 않았다. 따라서, 분자전자소자의 미래 상용화를 위해서는 신뢰할 수 있는 분자 전자 접합의 제조 및 전하 수송 특성의 조사가 요구된다.

이와 관련하여, 먼저 그래핀 전극으로 고수율 및 신뢰성 있는 벤젠다이티올 계열 분자 접합을 제작하고 전기적 특성을 조사하였다. 분자 접합의 길이 및 온도 의존적 전기적 특성을 연구했으며, 이로부터 주요 전도 메커니즘은 비 공진 터널링이라는 것을 밝혔다. 또한 외부 스트레스 환경에서 분자 접합의 신뢰성을 조사했다. 그런 다음 벤젠-1,4-다이티올 분자 접합의 진동 모드와 전하 수송 현상을 비탄성전자터널링분광법을 통해 측정하였다.

둘째, p-도핑 된 그래핀 전극 벤젠다이티올 분자 접합에 관한 연구를 수행했다. 그래핀 필름의 p-도핑은 프리스테인 그래핀(~ 4.40 eV의 일함수를 가짐)을 트리플루오로메탄설폰산으로 처리하여 이루어졌으며, 현저히 증가된 일함수 (~ 5.23 eV)를 얻어냈다. 이로부터, 트리플루오로메탄설폰산-그래핀 전극 분자 접합에서 전하 수송이 향상되었으며, 향상된 전하 수송 특성이 터널링

분자 접합에서 전하 주입 장벽이 낮아짐에 따른 것임을 확인하였다.

마지막으로, 그래핀 전극을 가진 다이에릴에텐 자기조립단분자박막으로 구성된 분자 접합을 제작하고 광스위칭 특성에 대하여 조사하였다. 다이에릴에텐은 중앙에 있는 고리가 열리고 닫힘에 따라 높은 전도 상태(닫힘 상태; ON) 및 낮은 전도 상태(열림 상태; OFF)를 형성하는 광스위칭 기능성 분자다. 그래핀 전극 다이에릴에텐 분자 접합의 단방향 광스위칭 현상을 발견하고 그 원인에 대해 분석했다.

Keywords: 분자 전자학, 자기조립단분자박막, 그래핀전극, 전하 수송 특성, 계면 공정, 광스위칭 분자 접합

Student Number: 2013-22993